Title	Spin-down of Solar-mass Protostars in Magnetospheric Accretion Paradigm
Author(s)	Takasao, Shinsuke; Kunitomo, Masanobu; Suzuki, K. Takeru et al.
Citation	The Astrophysical Journal. 2025, 980(1), p. 111
Version Type	VoR
URL	https://hdl.handle.net/11094/100435
rights	This article is licensed under a Creative Commons Attribution 4.0 International License.
Note	

Spin-down of Solar-mass Protostars in Magnetospheric Accretion Paradigm

Shinsuke Takasao[1] , Masanobu Kunitomo[2,3] , Takeru K. Suzuki[4,5] , Kazunari Iwasaki[6] , and Kengo Tomida[7]

[1] Department of Earth and Space Science, Graduate School of Science, Osaka University, Toyonaka, Osaka 560-0043, Japan
[2] Department of Physics, Kurume University, 67 Asahimachi, Kurume, 830-0011, Fukuoka, Japan
[3] Université Côte d'Azur, Observatoire de la Côte d'Azur, CNRS, Laboratoire Lagrange, Bd de l'Observatoire, CS 34229, 06304 Nice cedex 4, France
[4] School of Arts & Sciences, The University of Tokyo, 3-8-1, Komaba, Meguro, Tokyo, 153-8902, Japan
[5] Department of Astronomy, The University of Tokyo, 7-3-1, Hongo, Bunkyo, Tokyo, 113-0033, Japan
[6] Center for Computational Astrophysics, National Astronomical Observatory of Japan, Mitaka, Tokyo 181-8588, Japan
[7] Astronomical Institute, Tohoku University, Sendai, Miyagi 980-8578, Japan

Abstract

Stellar spin is one of the fundamental quantities that characterize a star itself and its planetary system. Nevertheless, stellar spin-down mechanisms in protostellar and pre-main-sequence stellar phases have been a long-standing problem in star formation theory. To realize the spin-down, previous axisymmetric models based on the conventional magnetospheric paradigm have had to assume massive stellar winds or produce highly time-variable magnetospheric ejections. However, this picture has been challenged by both numerical simulations and observations. With a particular focus on the propeller regime for solar-mass stars, we propose a new picture of stellar spin-down based on our recent 3D magnetohydrodynamic simulation and stellar evolution calculation. We show that failed magnetospheric winds, unique to 3D models, significantly reduce the spin-up accretion torque, which make it easier for the star to spin-down. Additionally, the amplitude of time variability associated with magnetospheric ejections is reduced by 3D effects. Our simulation demonstrates that the star spins down by generating a conical disk wind, driven by a rotating stellar magnetosphere. Our theoretical estimates, inspired by the numerical model, suggest that the conical disk wind is likely to play a crucial role in extracting stellar angular momentum during the protostellar phase. As magnetospheric accretion is expected to occur in other accreting objects such as protogiant planets, this study will also contribute to the understanding of the angular momentum of such objects.

Unified Astronomy Thesaurus concepts: Protostars (1302); Pre-main sequence stars (1290); Stellar magnetic fields (1610); Early stellar evolution (434)

1. Introduction

Stellar spin is a key parameter to determine stellar properties of solar-mass stars, such as the level of magnetic activities. The mechanism that regulates the stellar spin evolution has been one of the long-standing problems in star formation theory (see, e.g., J. Bouvier et al. 2014 for a review). Accreting stars receive not only mass but also angular momentum from the accretion flows, which increases the stellar angular momentum. In addition, stellar contraction via radiative cooling (the Kelvin–Helmholtz contraction) results in stellar spin-up if the stellar angular momentum is conserved or increases in response to accretion. However, observations show that most of the pre-main-sequence (pre-MS) stars are rotating at speeds much lower than their breakup velocity (e.g., W. Herbst et al. 2007), which implies that mechanisms to spin down the stars are operating effectively. The median value is approximately 10% of the breakup velocity (e.g., F. Gallet & J. Bouvier 2013). A very similar problem is also found for planetary-mass objects (M. L. Bryan et al. 2018). Therefore, the spin-down problem is a common issue for accretion in stellar- and planetary-mass regimes.

Many theoretical models have been proposed to describe accretion modes that can realize the slow stellar rotation in the magnetospheric accretion paradigm. In the magnetospheric paradigm, the stellar field truncates the inner disk at the so-called magnetospheric radius r_{mag} (e.g., L. Hartmann et al. 2016). A widely discussed idea is the "disk-locking" picture (P. Ghosh & F. K. Lamb 1979; M. Camenzind 1990; A. Koenigl 1991). We define the corotation radius, r_{cor}, as the radius at which the material in a Keplerian orbit corotates with the star. The standard disk-locking models assume that all the stellar field lines retain a closed magnetic geometry even at larger radii of $r \gg r_{\mathrm{cor}}$. Stellar field lines penetrating the disk outside r_{cor} rotate faster than the disk, which results in the generation of the spin-down torque on the star. The star will reach a state of spin equilibrium when the spin-up accretion torque balances with the spin-down magnetic torque (see also A. Collier Cameron & C. G. Campbell 1993; P. J. Armitage & C. J. Clarke 1996). In this paradigm, the spin equilibrium is realized when r_{cor} is close to but larger than r_{mag}. To achieve spin equilibrium in the classical T Tauri phase, standard models commonly require a stellar dipole field strength of ~ 1 kG. Some observations found correlation between the presence of disks and the stellar spin (S. Edwards et al. 1993; J. Bouvier et al. 1997), which appears to be consistent with the expectation of the disk-locking scenario (see also C. Fallscheer & W. Herbst 2006; L. Cieza & N. Baliber 2007; L. Venuti et al. 2017).

Despite some success, the standard disk-locking models have been challenged theoretically. D. A. Uzdensky et al. (2002) theoretically showed that a large portion of the stellar fields will inflate to open up due to the differential rotation between the star and disk, which results in the reduction of the spin-down torque (see also D. Lynden-Bell & C. Boily 1994).

S. Matt & R. E. Pudritz (2004) examined the disk-locking theory by taking this effect into account, finding that the modified theory fails to explain the stellar spin-down.

A critical issue of the disk-locking models is the lack of considerations of mass-loss processes. Protostars generally have collimated jets with a speed similar to the escape velocity in the vicinity of the star ($\sim$100 km s^{-1}; e.g., T. Ray et al. 2007). F. Shu et al. (1994) proposed an axisymmetric steady model to relate the stellar rotation and jet launching in the magnetospheric accretion paradigm, which has been called the X-wind model (see also E. C. Ostriker & F. H. Shu 1995; S. Mohanty & F. H. Shu 2008). Although the X-wind model has provided great insights about the star–disk interaction, it is now recognized that the model poses many difficulties. The X-wind model cannot be used for general spin-down arguments because the model assumes that the star will always accrete near its disk-locked state while keeping the relation $r_{\rm cor} \approx r_{\rm mag}$. The model hypothesizes the formation of magnetocentrifugally driven winds from the magnetospheric boundary, while no magnetohydrodynamic (MHD) simulations have found such X-winds. M. M. Romanova et al. (2009) pointed out that conical winds similar to X-winds can form, but the winds are nonsteady and driven by a combination of centrifugal and magnetic pressure gradient forces. J. Ferreira (2013) summarized some other critical issues in more detail.

Based on these experiences, theoretical studies have begun to carefully examine the roles of various winds and their temporal variability. R. V. E. Lovelace et al. (1999) analyzed the launching of conical winds from the magnetospheric boundary around a rapidly rotating star with $r_{\rm cor} < r_{\rm mag}$ (note the difference from the X-wind model). The regime is called a propeller regime (e.g., A. F. Illarionov & R. A. Sunyaev 1975; M. M. Romanova et al. 2018). They found that the spin-down torque by the conical disk winds or jets can be comparable to the spin-up torque due to accretion, although the result depends on the property of turbulent magnetic diffusivity. J. Ferreira et al. (2000) also argued the importance of such winds in a different magnetic configuration where magnetic reconnection plays a role (see also S. Hirose et al. 1997). Another approach is to focus on the stellar winds. By noting that a fraction of the stellar fields have to be open in magnetospheric accretion (G. V. Ustyugova et al. 2006), S. Matt & R. E. Pudritz (2005) proposed that the strong stellar wind powered by accretion will carry away the angular momentum along the open fields. In addition, C. Zanni & J. Ferreira (2013) performed nonsteady 2D axisymmetric MHD simulations and found that magnetospheric ejections can play a role in the stellar spin-down.

Although the above studies have greatly advanced our understanding of angular momentum flows around the star, the updated axisymmetric models still have faced some challenges. Two-dimensional MHD simulations have found that the stellar spin-down will be possible with the help of polar jets, conical disk winds, and/or magnetospheric ejections (M. M. Romanova et al. 2004; P. S. Lii et al. 2014; M. M. Romanova et al. 2018; L. G. Ireland et al. 2022). However, the stellar accretion rate in such simulations shows significant time variability when the star is in the propeller regime, which is inconsistent with observations, as discussed in F. Gallet et al. (2019). The strong stellar wind may spin down the star without producing significant time variability, but the stellar wind mass-loss rate ($\dot{M}_{\rm SW}$) required for the spin-down is problematic. The $\dot{M}_{\rm SW}$ of the accretion-powered

stellar wind should be smaller than $\sim$1% of the accretion rate $\dot{M}_{\rm acc}$ because of the energy constraint (S. R. Cranmer 2008; C. Zanni & J. Ferreira 2011). This is in contrast to the conclusion derived from 2D MHD models that the spin-down torque by the stellar wind can dominate the spin-up torque by accretion only if $\dot{M}_{\rm SW}$ is larger than approximately 10% of $\dot{M}_{\rm acc}$ (G. Pantolmos et al. 2020; L. G. Ireland et al. 2021).

We consider that the challenges highlighted above stem from the inherent limitations of 2D axisymmetric models. In reality, accreting flows interact with the rotating magnetosphere through nonaxisymmetric processes, such as turbulent mixing, which are not captured by axisymmetric models. The axisymmetric models necessitate assumptions about turbulent magnetic diffusivity to simulate penetration. G. V. Ustyugova et al. (2006) demonstrated that the mass-loss rate from conical disk winds varies significantly based on these model assumptions, complicating the assessment of different winds' roles in stellar spin-down. Furthermore, axisymmetric models maintain perfect coherency in the azimuthal direction, which is an assumption not upheld in 3D cases. MHD instabilities at the magnetospheric boundary, for example, can disrupt this coherency by facilitating accretion flows that penetrate the stellar magnetosphere (e.g., A. K. Kulkarni & M. M. Romanova 2008). To address these limitations, a transition to 3D modeling is necessary.

Recently, S. Takasao et al. (2022, hereafter ST22) performed 3D MHD simulations of magnetospheric accretion and presented a new picture of angular momentum transport in the magnetospheric accretion paradigm. We showed that a star in the propeller regime can spin down by driving a conical disk wind without showing a significant time variability in the accretion rate, which again highlights the importance of the conical disk wind. Considering the updates provided by our 3D MHD simulations, we derive the upper limit of the spin-down time. This study focuses on the spin-down torque by the conical disk winds driven by the rotating magnetosphere. We take into account the stellar evolution and estimate the upper limit of the spin-down time at each age. We show that the 3D effects of star–disk interaction are key to resolving the challenges of the stellar spin-down.

2. General Picture of Accretion and Ejection
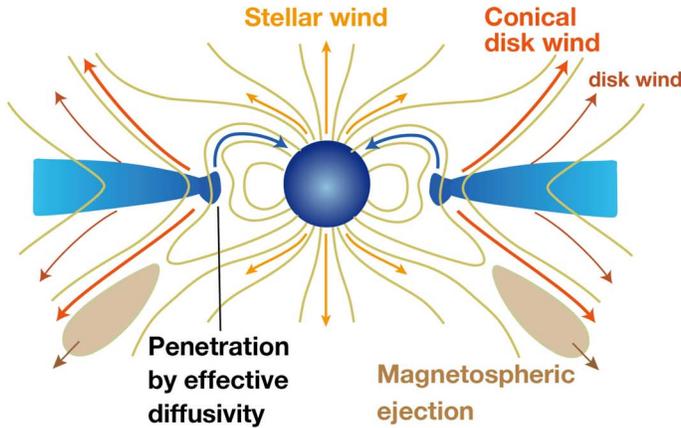
2.1. A Brief Review of 2D Models

As we are interested in the stellar spin-down, we only consider the propeller regime. We first review general properties of 2D models and then give an overview of key results of the 3D MHD simulation by ST22, with a particular focus on the 3D effects.

Previous 2D studies predict the following types of ejections (e.g., M. M. Romanova et al. 2018):
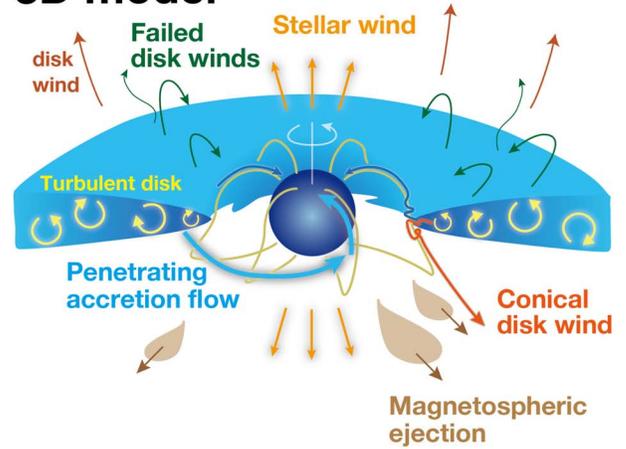
1. Stellar winds.
2. Magnetospheric ejections.
3. Disk winds.
   (a) Conical disk winds driven by star–disk interaction.
   (b) Disk winds driven by disk fields.

The left panel of Figure 1 illustrates the above structures. The stellar winds blow from the polar regions. If the protostar is in the strong propeller regime ($r_{\rm cor} \ll r_{\rm mag}$), the magnetically driven polar jet will also appear (M. M. Romanova et al. 2005). Magnetospheric ejections are plasma ejections associated with magnetic reconnection of the stellar magnetosphere

2D model

Stellar wind

Conical disk wind

disk wind

Penetration by effective diffusivity

Magnetospheric ejection

3D model

disk wind

Failed disk winds

Stellar wind

Turbulent disk

Penetrating accretion flow

Conical disk wind

Magnetospheric ejection

Figure 1. Schematic illustration of the accretion and ejection structures in 2D (left) and 3D (right) models. The illustration for the 3D model is based on the results of ST22.

(e.g., M. R. Hayashi et al. 1996; C. Zanni & J. Ferreira 2013). They occur when the stellar magnetic fields are sufficiently twisted by the differential rotation between the protostar and disk gas (e.g., D. Lynden-Bell & C. Boily 1994). Note that in the 2D models the reconnection region extends in the azimuthal direction as a ring owing to the axisymmetry. As a result, the magnetospheric ejections take the form of a torus-like structure. In the magnetosphere–disk interface, disk gas penetrates in response to an effective diffusivity that imitates the turbulent diffusion. A fraction of the penetrating flow accretes onto the protostar, while the rest of it is expelled away as conical disk wind by the rotating stellar magnetic fields. The conical disk winds often show a north–south asymmetric structure (e.g., P. S. Lii et al. 2014), where accretion occurs in one hemisphere and ejections can proceed in the other hemisphere. The conical disk wind will be surrounded by the disk wind driven by the disk fields.

In the propeller regime, the protostar is expected to expel the angular momentum to the disk gas via the magnetosphere–disk interaction. However, a quantitative conclusion is difficult to draw due to some assumptions. Previous studies investigated the mass and angular momentum transfer by commonly assuming that the magnetosphere is nearly rigidly rotating with the protostar (e.g., R. V. E. Lovelace et al. 1999; G. V. Ustyugova et al. 2006; C. R. D'Angelo & H. C. Spruit 2010). However, the rotation profile of the magnetosphere depends on the details of the twisting of the magnetosphere through the magnetosphere–disk interaction (e.g., W. Kluźniak & S. Rappaport 2007). We also note that the bifurcation of the accretion and ejection is sensitive to the adopted diffusivity model (G. V. Ustyugova et al. 2006). The mass loading to the magnetosphere in the 2D models occurs through the effective diffusivity, which imitates turbulent mixing (e.g., F. Shu et al. 1994). (We note that magnetic reconnection between the magnetosphere and disk fields can provide another path of mass loading; see, e.g., S. Hirose et al. 1997; J. Ferreira et al. 2000). However, details about the (effective) magnetic diffusivity remain poorly understood. Therefore, it is necessary to examine the assumption about the rigid rotation and the properties of the turbulent mixing using 3D MHD simulations.

The accretion torque $\dot{J}_{\mathrm{acc}}$ is commonly approximated as (e.g., S. Matt & R. E. Pudritz 2005)

$$\dot{J}'_{\mathrm{acc}} = \dot{M}\sqrt{GM_* r_{\mathrm{mag}}}, \qquad (1)$$

where $\dot{M}$ is the rate of mass accretion onto the protostar, G is the gravitational constant, and M_* is the protostellar mass. The above estimate is based on the assumption that the accreting flows bring the angular momentum which they have at the magnetospheric boundary to the protostar. However, 2D MHD simulations find that the winds emanating from the magnetospheric boundary carry away a part of the angular momentum of the accretion flows (C. Zanni & J. Ferreira 2013; L. G. Ireland et al. 2021). Therefore, it is reasonable to use the expression $\dot{J}_{\mathrm{acc}} = K_{\mathrm{acc}} \dot{J}'_{\mathrm{acc}}$ for a more realistic accretion torque, where $0 \leqslant K_{\mathrm{acc}} \leqslant 1$. Previous 2D models find a reduction of the spin-up torque by a few tens of percent: $K_{\mathrm{acc}} \approx 0.7$–$0.8$ (C. Zanni & J. Ferreira 2013; L. G. Ireland et al. 2021).

2D models predict that accretion in protostars in the propeller regime may cease and occur in an episodic way, which seems to be inconsistent with observations. Although the star–disk interaction in 2D depends on the adopted diffusivity models, G. V. Ustyugova et al. (2006) suggest that powerful outflows can almost quench accretion in the propeller regime. However, protostars systematically show higher accretion rates than T Tauri stars (e.g., E. Fiorellino et al. 2021), which raises a question about the accretion quenching. Time-variable accretion is also a common result of 2D models. The accretion rate can change by an order of magnitude as a result of magnetospheric ejections (M. M. Romanova et al. 2004; P. S. Lii et al. 2014). C. Zanni & J. Ferreira (2013) and L. G. Ireland et al. (2022) clarify the importance of magnetospheric ejections for stellar spin-down, and some observations indeed find indications of ejections (J. Bouvier et al. 2023). However, observations do not commonly find such strong variability, challenging our understanding based on 2D models. The above challenges motivate us to perform 3D simulations.

2.2. An Overview of the 3D Model of ST22

Figure 2 presents a snapshot of our 3D simulation (Model A of ST22). The accretion disk is turbulent in response to
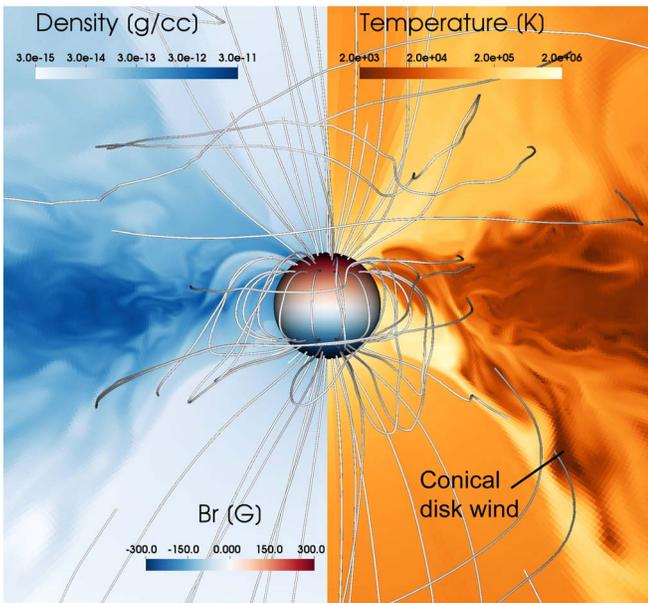
Figure 2. Accretion and wind structures of the 3D MHD simulation (Model A of ST22; $r_{cor} = 1.5R_*$ and $r_{mag} \approx 2.5R_*$). The left and right panels show density and temperature cutouts, respectively. Lines denote magnetic field lines. The stellar surface is colored with the radial component of the magnetic fields.

magnetorotational instability (MRI; S. A. Balbus & J. F. Hawley 1991). Therefore, we can study the magnetosphere–disk interface without assuming an effective diffusivity, although we still require a convergence check of the results by performing higher-spatial-resolution simulations. The ejections found in previous 2D models also appear in the model: namely stellar winds, magnetospheric ejections, and asymmetric conical disk winds. The 3D model further exhibits additional types of winds. A key distinction between the 2D and 3D models lies in the presence of turbulence and nonuniform structures in the azimuthal direction. Asymmetric jets are indeed commonly observed in young protostars (L. Podio et al. 2021), which seems to provide observational support to our model.

In three dimensions, the mass loading to the magnetosphere is mediated not only by the turbulent mixing but also the penetration of filamentary flows. Figure 3 presents an example of filamentary accretion flows penetrating into the magnetosphere. A schematic illustration is given in the right panel of Figure 1. It has been recognized that similar unstable magnetospheric accretion occurs in slowly rotating stars as a result of magnetic Rayleigh–Taylor instability (A. K. Kulkarni & M. M. Romanova 2008; A. A. Blinova et al. 2016), but the stability in the propeller regime was unclear. ST22 showed that penetrating accretion flows can also form even in the case of the propeller regime, though in response to different instabilities (probably the magnetogradient-driven instability; K. Hirabayashi & M. Hoshino 2016). The difference in the stellar spin rate appears in the thickness of the filaments: Filaments in the propeller regime are thicker than those in slow rotators. We can understand the result as that the velocity shear in the magnetosphere smears out their small-scale structure. The formation of penetrating flows prevents the accumulation of mass at the magnetospheric edge and suppresses the amplitude

of time variability in accretion, which is distinct from the 2D models.

The penetrating flows drag the disk toroidal fields, which allows them to continuously transport their angular momentum to the disk gas. Figure 3 displays some field lines threading the flow. The field lines go through the midplane and extend to the other side of the disk. As can be seen, magnetic fields in the penetrating flows are connected with the protostar, probably because they experience magnetic reconnection with the stellar field. Note that the field lines are trailing with respect to the stellar rotation, which indicates that the penetrating flow is efficiently losing angular momentum. The trailing fields also exert spin-down torque onto the protostar.

The penetrating flows are often accompanied by slowly outgoing flows as a back-reaction of accretion. The radial speed of the accelerated gas is considerably smaller than the escape velocity. Therefore, the outflows will fail to escape from the stellar gravity. We categorize these as a type of "failed magnetospheric winds." In ST22, we describe them as a type of turbulent winds because of their disturbed structures. However, as the penetrating flows have coherent structures, they are not necessarily turbulent. A more detailed analysis of the angular momentum flows is presented in Appendix A.

We identify another type of failed magnetospheric winds associated with MRI turbulence. Three-dimensional MHD simulations have commonly found turbulent disk winds above MRI-turbulent disks (e.g., T. K. Suzuki & S.-i. Inutsuka 2009; X.-N. Bai & J. M. Stone 2013; S. Takasao et al. 2018). As their acceleration is inefficient due to their turbulent nature, most of the winds fail to escape (indicated as green arrows in Figure 1). When they fall, they continuously shear the magnetic field and increase the Maxwell stress. The continuous growth of the Maxwell stress leads to a runaway removal of angular momentum from the accreting material. As a result, failed winds can form patchy accretion streams with a velocity similar to the free-fall velocity (S. Takasao et al. 2018). The mechanism of the angular momentum loss is similar to the onset of MRI and the other type of failed magnetospheric winds (see also Z. Zhu & J. M. Stone 2018; J. Jacquemin-Ide et al. 2021 for similar flows at larger scales). The failed disk winds drive outflows when they fall as a back-reaction of angular momentum loss. ST22 demonstrate that the failed winds also form just around the turbulent magnetosphere–disk interface. The failed winds hit the magnetosphere and become a part of the magnetospheric funnel accretion flows.

Figure 4 presents a schematic illustration of the failed magnetospheric winds. The two types of winds are shown: the failed winds associated with a penetrating flow, and the failed winds emanating from the turbulent magnetosphere–disk interface (see also Figure 3 regarding the field structure of penetrating flows). The difference between the two types of winds lies in the mechanisms which produce the accretion streams. The penetrating flows are created by MHD instabilities at the magnetospheric boundary, while the patchy structure of the winds from the magnetospheric boundary is formed by the disk turbulence. In both cases, accreting flows experience runaway angular momentum loss by twisting the magnetic fields. As a result, the rate at which angular momentum is injected into the protostar is significantly lower than the classical estimation ($\dot{J}'_{acc}$). The simulation suggests that $K_{acc} = 0.1$ is a reasonable choice, although this value may
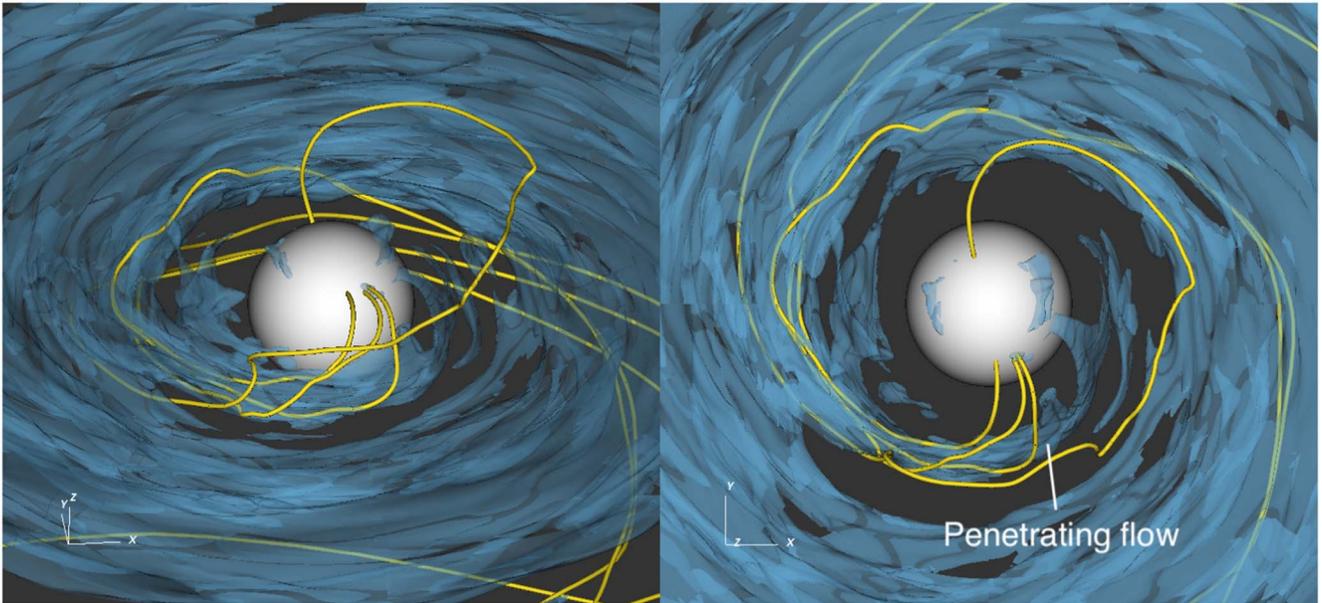
Figure 3. An example of filamentary accretion flows penetrating into the magnetosphere ($t = 151.1$ days of Model A of ST22). The structure is viewed from two different points of view. The density isosurface is colored in blue. Four field lines threading the penetrating flow are denoted as yellow lines.
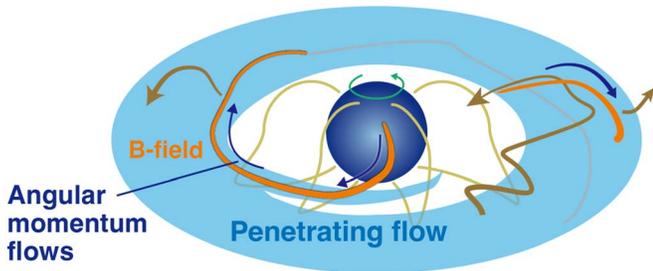
Figure 4. A schematic illustration of the two types of failed magnetospheric winds. Orange lines denote magnetic field lines associated with failed winds. Brown lines with arrows indicate failed winds. Dark blue arrows show the flow of angular momentum along field lines.

evolve in response to the stellar and disk evolution, which needs to be investigated in future studies.

The rotation profile of the magnetosphere is found to be different from expectations based on 2D models because of the presence of penetrating flows (see Section 3.4 of ST22). The penetrating flows which form around the midplane have a substantial inertia. After penetration, the dense flows persist in rotating for a few orbits before ultimately descending to the protostar, despite the effects of magnetic braking. As a result, they force a large body of the magnetosphere to rotate nearly at Keplerian velocity. Therefore, the assumption of rigid rotation inside the magnetosphere is found to be invalid. Rather, Keplerian rotation in the magnetosphere–disk interface seems to be a better assumption (the assumption of rigid rotation will be valid in the case that the accretion rate is so small that penetrating flows cannot affect the rotational profile of the magnetosphere). W. Kluźniak & S. Rappaport (2007) also investigated a smooth transition of the rotational profile from a Keplerian disk to a rotating star. Their analytical solutions indeed show a similar near-Keplerian rotation in the outer magnetosphere. However, their analytical solutions do not match the result of our 3D models, probably because their

analytical model lacks 3D effects such as the forced rotation by penetrating flows and the vertical transport of angular momentum by stellar fields.

The role of magnetospheric ejections in stellar spin-down seems to be limited in 3D, although they play critical roles in 2D models. Our 3D model does not show significant time variability in the accretion rate even though magnetospheric ejections occur, which indicates that magnetospheric ejections are not as violent as found in 2D models. The difference is related to the penetrating flows. In 2D models, the stellar magnetosphere can be coherently twisted by the rotating gas that accumulates at the magnetospheric boundary. However, in 3D the gas does not accumulate at the magnetospheric boundary but forms penetrating flows. The penetrating flows cannot twist the magnetosphere coherently because they only twist a part of the stellar magnetosphere. The resulting magnetospheric ejections are patchy in the azimuthal direction (Figure 1), which results in a weaker energy release than in 2D cases (see ST22 for more reasons why it is difficult for powerful magnetospheric ejections to occur in 3D).

We also note that, in Model A of ST22, distinguishing between magnetospheric ejections and conical disk winds is difficult in many cases. The conical disk wind itself shows a significant density inhomogeneity (Figure 2), probably because the turbulent disk gas is accelerated by fluctuating fields. In addition, magnetospheric ejections with coherent structures are uncommon. For these reasons, we include magnetospheric ejections as a part of the conical disk winds in our analysis. We consider that this treatment will not significantly affect our arguments about the conical disk winds as long as the time variability is insignificant.

In summary, the nonuniform magnetospheric structure in the azimuthal direction (including turbulence) is key to explaining the spin-down of protostars showing a low level of variability. The nonuniform structure allows accretion and ejection to occur simultaneously. Because of the "traffic control" of mass and angular momentum flows, the 3D model shows a much lower level of variability than 2D models. Accretion flows

around the magnetosphere take filamentary or patchy structures. They lose a large fraction of angular momentum during their fall in a runaway manner, which results in a reduction of the spin-up torque by accretion. The filamentary penetrating flows force the magnetosphere to rotate nearly at Keplerian speed, which indicates that Keplerian rotation of the magnetosphere is a more realistic assumption than rigid rotation around the magnetosphere–disk interface. Torus-like magnetospheric ejections found in 2D models are rare in 3D because of the localization of magnetic reconnection regions in the azimuthal direction, which suggests that their role in stellar spin-down should be limited in 3D. Therefore, we focus on the spin-down torque by conical disk winds.

3. Modeling Spin-down Torque by Conical Disk Winds

In general, the spin-down torque by a magnetically driven wind can be estimated as follows:

$$\dot{J}_{\mathrm{wind}} \approx \dot{M}_{\mathrm{wind}} r_{\mathrm{A}}^2 \Omega(r_0), \tag{2}$$

where $\dot{M}_{\mathrm{wind}}$ is the wind mass-loss rate, r_{A} denotes the Alfvén radius, and $\Omega(r_0)$ is the angular velocity of the magnetic field at the radius of the wind base $r = r_0$ (e.g., I. Pascucci et al. 2023). The Alfvén radius indicates the size of the so-called Alfvén surface, where the poloidal velocity of the plasma flow is equal to the poloidal Alfvén velocity. The magnetic field inside the Alfvén surface nearly rigidly rotates with the star. To calculate the spin-down torque, we need to estimate each component on the right-hand side of Equation (2).

We consider a more specific functional form of Equation (2) for the conical disk winds. Considering that a large portion of the magnetosphere rotates nearly at Keplerian velocity because of the penetrating accretion flows, the rotation rate of the magnetosphere at the magnetosphere–disk interface will reach nearly a Keplerian value there, $\Omega_{\mathrm{K}}(r_{\mathrm{mag}})$. Namely, $\Omega(r_0) = \Omega_{\mathrm{K}}(r_{\mathrm{mag}})$, which is distinct from the common assumption of rigid rotation, $\Omega(r_0) = \Omega_*$. This eliminates the explicit dependence of the stellar spin rate on the spin-down torque (Equation (2)).

The Alfvén radius r_{A} for conical disk winds will be comparable to or larger than the magnetospheric radius because the mass loading mainly occurs at $r = r_{\mathrm{mag}}$. Indeed, it is of order a few r_{mag} in Model A of ST22 (see Appendix B). To clarify the relation between the two, we write r_{A} as $r_{\mathrm{A}} = f_{\mathrm{A}} r_{\mathrm{mag}}$, where f_{A} is a nondimensional value that is larger than unity. The functional form of f_{A} will depend on relevant quantities such as the stellar spin rate and mass-loss rate. In this study, we follow the suggestion by J. Ferreira et al. (2000) to consider a possible range of f_{A}. Considering observations of jets and an analytical solution of disk winds based on J. Ferreira (1997), J. Ferreira et al. (2000) inferred that the magnetic lever arm λ, which is defined as $r_{\mathrm{A}}^2 \approx \lambda r_{\mathrm{cor}}^2$, will be in the range of $2 \lesssim \lambda \lesssim 7$. We note the relation $f_{\mathrm{A}}^2 / \lambda = (r_{\mathrm{cor}}/r_{\mathrm{mag}})^2$. The range corresponds to $1 \lesssim f_{\mathrm{A}} \lesssim 3$ in the case of a weak propeller regime ($r_{\mathrm{mag}} \approx r_{\mathrm{cor}}$). The value of f_{A} may be close to unity in the case of a strong propeller regime owing to a high mass-loss rate. Despite uncertainties about the magnetic lever arm, the value of f_{A} seems to be limited in a small range. Therefore, in this study we assume that the value can be approximated as a constant when the protostar drives the conical disk winds and we adopt $f_{\mathrm{A}} = 2$ as a fiducial value. This assumption needs to be examined in future studies.

The spin-down torque by conical disk wind driven from the magnetospheric boundary can then be estimated as

$$\dot{J}_{\mathrm{CDW}} \approx f_{\mathrm{A}}^2 \dot{M}_{\mathrm{CDW}} r_{\mathrm{mag}}^2 \Omega_{\mathrm{K}}(r_{\mathrm{mag}}), \tag{3}$$

where $\dot{M}_{\mathrm{CDW}}$ denotes the mass-loss rate of the conical disk wind. We introduce the wind mass-loss efficiency f_{eff} such that $\dot{M}_{\mathrm{CDW}} = f_{\mathrm{eff}} \dot{M}_{\mathrm{acc}}$, where $0 < f_{\mathrm{eff}} < 1$ and $\dot{M}_{\mathrm{acc}}$ is the accretion rate onto the star. In Model A of ST22, $f_{\mathrm{eff}} \approx 0.1$–$0.2$, which seems to be similar to observational estimations of the efficiency (e.g., T. Ray et al. 2007). The efficiency will be determined by the details of the mass loading to the magnetosphere, which will depend on the property of turbulence and the stellar and disk parameters. Nevertheless, we theoretically infer that $\dot{M}_{\mathrm{CDW}} \propto \dot{M}_{\mathrm{acc}}$ and $f_{\mathrm{eff}} = \mathcal{O}(0.1)$, as argued in Appendix C. Considering the numerical result, we adopt $f_{\mathrm{eff}} = 0.2$ as a fiducial value here. We also compare the mass loading between a stellar wind and a conical disk wind in Appendix D to emphasize the importance of the conical disk winds.

This study uses Equation (3) to estimate the upper limit of the spin-down time of the protostar in the propeller regime, by considering that conical disk winds are the main carrier of stellar angular momentum. ST22 showed that conical disk winds are continuously blowing in propeller regimes, while they are intermittent and sometimes absent in nonpropeller regimes (Model B and C in ST22), which implies that f_{eff} depends on the stellar spin. This result limits our discussion to the propeller regime only. This study further assumes that a protostar will reach a spin equilibrium once it decelerates to a point where $r_{\mathrm{cor}} \approx r_{\mathrm{mag}}$ as a result of the balance between the spin-up and spin-down torques. M. Long et al. (2005) suggested that, in 2D simulations, $r_{\mathrm{cor}} \approx f_{\mathrm{cor,eq}} r_{\mathrm{mag}}$ in the spin-equilibrium state, where $f_{\mathrm{cor,eq}} = 1.3$–$1.5$ (see also J. Bouvier et al. 2007). We note that the value of $f_{\mathrm{cor,eq}}$ might differ in 3D models. The details of achieving a spin equilibrium, however, is beyond the scope of this study. Considering the uncertainties in the current understanding, we choose $f_{\mathrm{cor,eq}} = 1$ for calculating the angular momentum of a protostar in spin equilibrium.

A protostar in spin equilibrium may reenter the propeller regime by spinning up in response to the disk and stellar evolution. In this case, we consider that the protostar will again start to blow continuous conical disk winds and spin down itself. We also estimate the spin-down timescale for this case by assuming that the protostellar spin rate is close to the value in spin equilibrium.

4. Stellar Evolution Model

To compute the spin-down timescale across different stellar ages, it is necessary to calculate key stellar parameters, such as the radius and moment of inertia, for an accreting star. We utilize the Modules for Experiments in Stellar Astrophysics (MESA) code to simulate the evolution of a young accreting star to facilitate these calculations. However, it is important to note that this study is designed to estimate the upper limit of the spin-down time at various stellar ages. For simplicity, we employ MESA solutions that do not account for the effects of stellar rotation as references, thereby omitting the calculation of long-term spin evolution. Assumptions regarding the stellar magnetic field, such as the stellar dynamo and the removal of

fossil fields, will influence the initial conditions for spin evolution (e.g., S. Takasao et al. 2019). Additionally, the size of the stellar magnetosphere, which may vary with the disk's magnetic field, remains poorly understood (e.g., J. Ferreira et al. 2000). Given these complexities, a detailed analysis of long-term spin evolution is reserved for future studies. This section provides brief explanations of our methods. For more detailed descriptions, readers are referred to Appendix E.

The accretion rate $\dot{M}_{acc}$ is a function of time (stellar age), t_{age}. We assume a constant rate of $\dot{M}_{acc} = 10^{-5} M_\odot \, \mathrm{yr}^{-1}$ until 3.1×10^4 yr. After that, it decreases as

$$\dot{M}_{acc} \propto t_{age}^{-a}, \tag{4}$$

where $a > 0$ is a measure of the rapidity of the decrease in the accretion rate. Considering the estimation by L. Hartmann et al. (1998), we adopt $a = 3/2$ as a fiducial value. The resulting final mass of the star is $1\,M_\odot$, which is achieved at $t = 10$ Myr. We have confirmed that our conclusions are insensitive to the choice of the index a (Appendix E).

We assume that the dipole magnetosphere is established in a sufficiently early phase (possibly $\lesssim 0.1$ Myr). The magnetospheric radius r_{mag} is calculated using the equation derived in ST22, a modified version of the Ghosh & Lamb relation (P. Ghosh & F. K. Lamb 1979):

$$\begin{aligned}
\frac{r_{mag}}{R_*} &= \left(\frac{\eta'^2 \mu_*^4}{4 G M_* \dot{M}^2}\right)^{1/7} \\
&\approx 6.6 \left(\frac{\eta'}{1}\right)^{2/7} \left(\frac{B_*}{1 \ \mathrm{kG}}\right)^{4/7} \left(\frac{R_*}{2 R_\odot}\right)^{5/7} \\
&\quad \times \left(\frac{M_*}{0.5 M_\odot}\right)^{-1/7} \left(\frac{\dot{M}}{10^{-8} M_\odot \ \mathrm{yr}^{-1}}\right)^{-2/7},
\end{aligned} \tag{5}$$

where η' denotes a twist of the magnetic fields. The detailed dependence of η' on the thermal property of the disk gas needs to be investigated in future studies, but we set the value to unity for a conservative discussion. ST22 derived the above equation very similarly to the Ghosh & Lamb relation using the angular momentum transfer equation. We note that the magnetospheric radius in this study is defined as an azimuthally averaged quantity for the disturbed magnetosphere (see also A. A. Blinova et al. 2016; S22). Equation (5) approximately agrees with the results of ST22. Observations indicate that CTTSs generally host kilogauss surface magnetic fields (e.g., C. P. Johnstone et al. 2014). The field strength is comparable to or larger than the field strength determined by the pressure balance between the surface gas pressure and the magnetic pressure (P. N. Safier 1999; C. M. Johns-Krull 2007). Considering the observations, we adopt 1–2 kG as a typical value of the stellar field. We assume that the above formula is valid in the propeller regime.

The dipole field assumption seems reasonable, particularly for young and rapidly rotating T Tauri stars (S. G. Gregory et al. 2012). Magnetic obliquity will affect the inner disk structure when the inclination angle is greater than a few tens of degrees (M. M. Romanova et al. 2003). However, observations suggest that the majority of stars show an inclination angle of $\sim 10°$ only (P. McGinnis et al. 2020). Therefore, we ignore the effects of misalignment and discuss the spin-down process based on our 3D model (ST22), where the axis of the dipole field is aligned with the rotation axis.

When we calculate the stellar angular momentum, we take two angular speeds as references. One is the maximum stellar spin, and the other is the value for a spin-equilibrium state. M.-K. Lin et al. (2011) suggest that gravitational torques prevent a protostar from spinning up to more than half of its breakup velocity. Considering their result, we take the maximum angular velocity of the protostar, $\Omega_{*,max}$, as $0.5\Omega_{br}$, where $\Omega_{br} = \sqrt{G M_*/R_*^3}$ is the breakup angular speed. When a protostar is in spin equilibrium ($r_{cor} = f_{cor,eq} r_{mag}$ and $f_{cor,eq} \approx 1$), the stellar angular velocity is estimated to be $\Omega_{*,eq} = f_{cor,eq}^{-3/2} \Omega_K(r_{mag})$. In this study, to define the propeller regime, we simply assume that $f_{cor,eq} = 1$ in a spin equilibrium. The detailed condition of spin equilibrium is beyond the scope of this study.

5. Upper Limit of the Spin-down Time

We first describe the general evolution of key stellar quantities. Panel (a) of Figure 5 displays the evolution of the accretion rate (see Equation (4)). The stellar radius evolves in response to accretion and Kelvin–Helmholtz contraction, as shown in the panel (b). We also plot a line of $R_* \propto t_{age}^{-1/3}$ as a reference, which is predicted for a star on the Hayashi track. This scaling is particularly relevant to the period $t_{age} \gtrsim 0.5$–1 Myr in our model. Before the Hayashi phase, the stellar radius slightly increases due to deuterium burning in the period spanning 0.1 to 0.3 Myr. Panel (b) also shows the evolution of r_{mag}. In the case of $B_* = 1$ kG, $r_{mag} \approx 20 R_\odot$ at $t_{age} = 0.3$ Myr. As R_* and r_{mag} decline approximately similarly during 0.3–1 Myr, we can approximate r_{mag}/R_* as a constant in this period. The detailed functional form is shown in Appendix E. After approximately 1 Myr, the magnetospheric radius declines more slowly than the stellar radius because of reduction of the accretion rate (Equation (5)). The stellar moment of inertia I_* also decreases in response to the reduction in the stellar radius (panel (c)). In the plot, I_* is normalized by $I_0 = M_\odot R_\odot^2$. k_*^2 is the moment of inertia normalized as follows: $k_*^2 = I_*/M_* R_*^2$. The figure shows that k_*^2 is nearly constant in the period of interest, suggesting that $I_* \propto M_* R_*^2$.

Panels (d)–(f) of Figure 5 display the evolution of the quantities of the stellar spin at a maximum spin rate and in a hypothetical spin equilibrium where $r_{cor} = r_{mag}$ is assumed. Panel (d) shows the stellar rotation periods in the two states. The period of ~4 days in the state with $r_{cor} = r_{mag}$ is similar to observed values for T Tauri stars (J. Bouvier et al. 2014). The corresponding stellar angular momenta are indicated in panel (e). We write the maximum stellar angular momentum as $J_{*,max} = I_* \Omega_{max}$ and the angular momentum of a star in spin equilibrium as $J_{*,eq} = f_{cor,eq}^{-3/2} I_* \Omega_K(r_{mag})$. In this study, we focus on young fast rotators and thus assume that the core and envelope rotate at the same velocity (e.g., F. Gallet & J. Bouvier 2013). Figure 5(f) shows $\dot{J}_{CDW}$ calculated using Equation (3). $\dot{J}_{CDW}$ declines as time proceeds because the mass-loss rate $\dot{M}_{CDW}$ and the rotating arm $f_A r_{mag}$ decrease. Therefore, we expect a strong angular momentum loss in the early phase, as argued by J. Ferreira et al. (2000).

We calculate the spin-down time t_{sd} for the case that the stellar angular momentum is extracted only by a conical disk wind emanating from the magnetospheric boundary. t_{sd} is
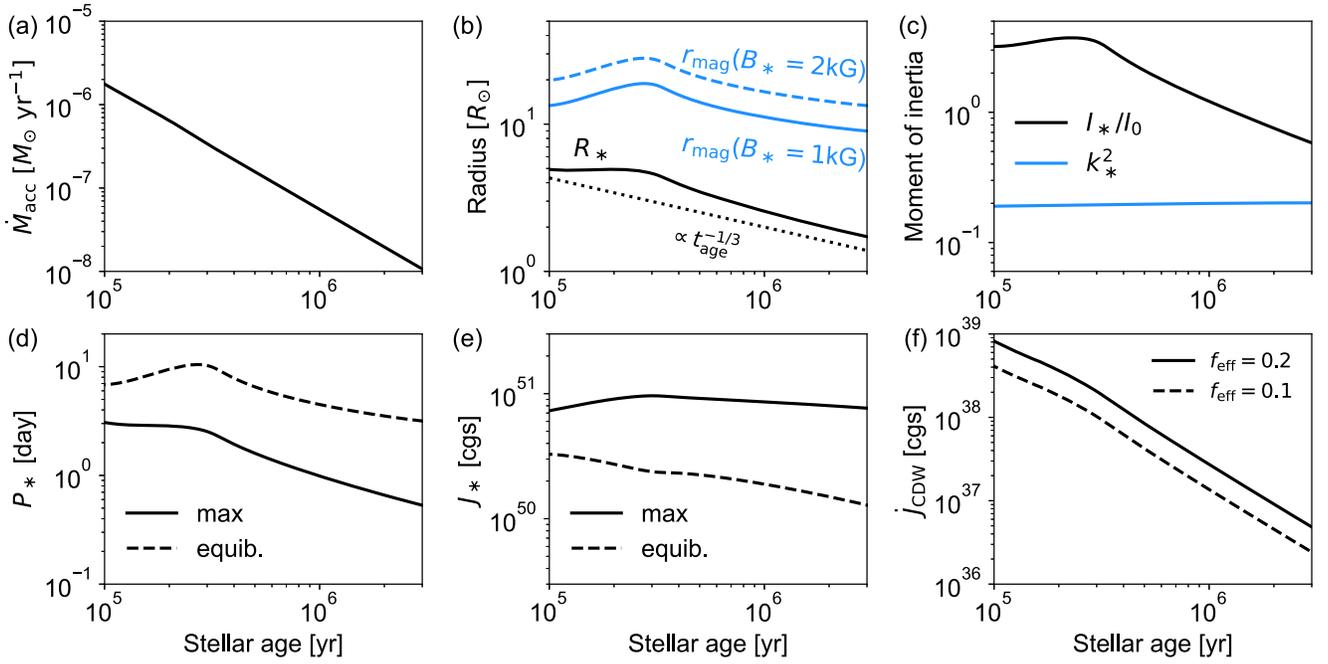
Figure 5. Evolution of key quantities. Panel (a): the stellar accretion rate. Panel (b): the stellar radius (black solid line) and the magnetospheric radius (blue solid and dashed lines). Panel (c): the moment of inertia; the black and blue lines show I_*/I_0 and k_*, respectively. Panel (d): the rotational periods for maximum rotation (solid) and in a hypothetical spin-equilibrium state (dashed), where $r_{cor} = r_{mag}$ is assumed. Panel (e): the stellar angular momenta for maximum rotation (solid) and in a hypothetical spin-equilibrium state (dashed). Panel (f): the spin-down torque by a conical disk wind ($B_* = 1$ kG).

estimated as

$$t_{sd} = \frac{J_*}{\dot{J}_{CDW}}. \tag{6}$$

The upper limit of the spin-down time corresponds to the case that the stellar angular momentum is $J_* = J_{*,max}$. We denote the upper limit as $t_{sd,up} = J_{*,max}/\dot{J}_{CDW}$. If other spin-down mechanisms such as massive stellar winds are important, the spin-down time will be smaller. Here, we ignore the contribution of the spin-up torque by accretion. As we will see later, this assumption seems to be valid as long as the spin-up torque is significantly reduced by failed magnetospheric winds, as seen in the 3D simulation (Section 2.2).

The upper limit of the spin-down time, $t_{sd,up}$, is shown in Figure 6. For the fiducial case of $f_{eff} = 0.2$ and $B_* = 1$ kG, the spin-down time is smaller than the stellar age in the range $t_{age} \lesssim 1$ Myr. This result demonstrates that a conical disk wind can significantly slow down a protostar before $t_{age} = 1$ Myr. The result only weakly depends on the stellar field strength. The efficiency of the conical disk winds (f_{eff}) has a stronger impact on the spin-down time (compare the dashed and solid lines). Our estimation presented here corresponds to an update of the previous estimation by A. Koenigl (1991). We also derive the scaling relations of $t_{sd,up}$ at the pre-MS stage, which is presented in Appendix F.

To illustrate the significance of the spin-down torque by conical disk winds, we compare it with other possible spin-down torques discussed by previous studies:

1. The torque by stellar wind, $\dot{J}_{SW}$.
2. The torque by magnetospheric ejection, $\dot{J}_{ME}$.

As they depend on the stellar spin rate, a direct comparison requires a detailed calculation of the time evolution of the stellar spin rate. As this is beyond the scope of this study, we
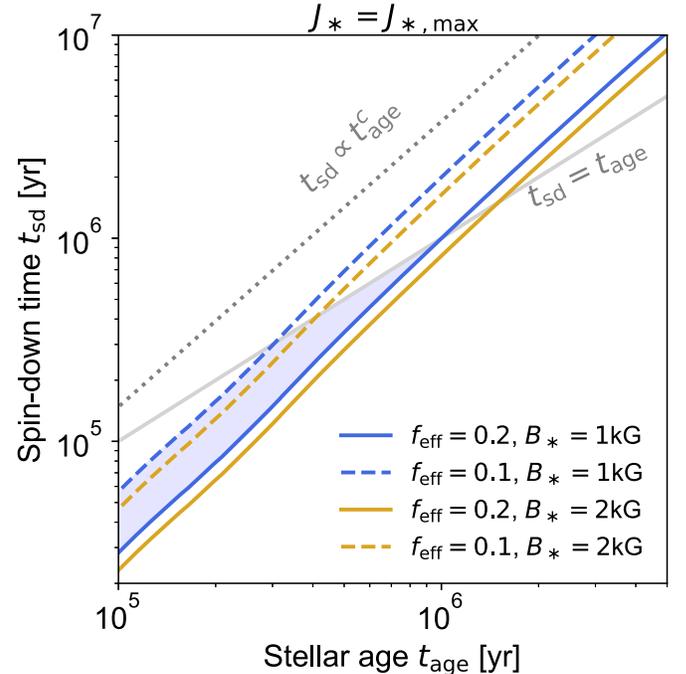
Figure 6. The spin-down time t_{sd} for a star rotating at $\Omega_* = 0.5\Omega_{br}$ (therefore, $t_{sd,up}$). The fiducial model is indicated by the solid blue line. The region where the spin-down time for the models with the fiducial field strength (1 kG) is shorter than the stellar age is filled with blue. The gray solid line shows the line for $t_{sd} = t_{age}$. The dotted line shows a scaling of $t_{sd} \propto t_{age}^c$, where $c = 59/42 \approx 1.4$.

calculate these torques in a propeller regime by assuming that $r_{cor} = 0.8 r_{mag}$.

We briefly describe the calculation methods for the above two torques. We provide detailed expressions for $\dot{J}_{SW}$ and $\dot{J}_{ME}$ in Appendix G. For the mass-loss rate of the stellar wind, $\dot{M}_{SW}$,
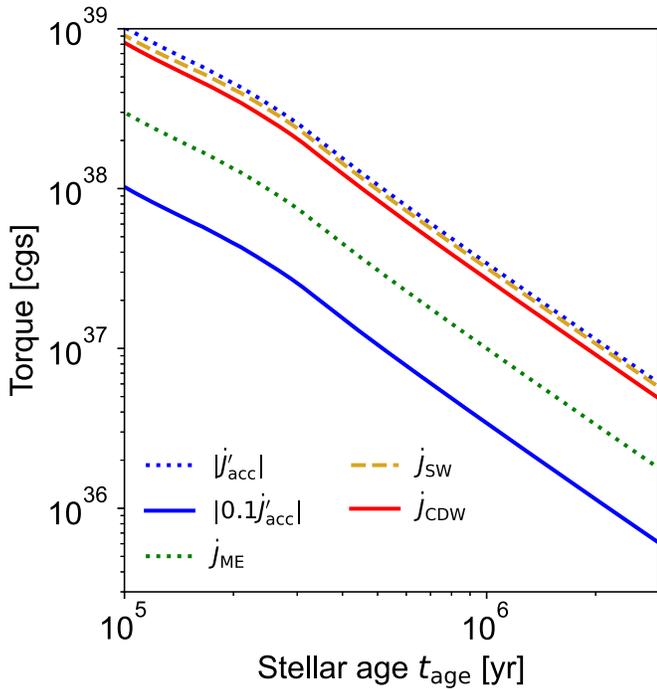
Figure 7. Different torques being exerted on a star with $r_{cor} = 0.8r_{mag}$ (a reference state of the propeller regime). The red line shows the torques by the conical disk wind. The blue dotted line indicates the accretion torque based on the simple estimation, $\dot{J}'_{acc}$. The blue solid line denotes $0.1\dot{J}'_{acc}$, an accretion torque that takes into account the angular momentum extraction by some winds. Other torques are also plotted for comparison. The green dotted line shows the spin-down torque by magnetospheric ejections. The dashed golden line denotes the spin-down torque by stellar wind in the case that $\dot{M}_{SW} = 0.1\dot{M}_{acc}$.

we assume $\dot{M}_{SW} = f_{SW}\dot{M}_{acc}$ and $f_{SW} = 0.1$, which would be a minimum value for the stellar wind to spin down the protostar (e.g., F. Gallet et al. 2019; L. G. Ireland et al. 2021). We note that this high efficiency (~10%) seems to be difficult to realize in reality (S. R. Cranmer 2008; C. Zanni & J. Ferreira 2011). For $\dot{J}_{ME}$, we adopt the analytical expression of F. Gallet et al. (2019) based on axisymmetric models (M. Livio & J. E. Pringle 1992; P. J. Armitage & C. J. Clarke 1996; S. Matt & R. E. Pudritz 2005). We note that the magnitude of the torque could be highly overestimated because of the axisymmetric assumption (see Section 2.2). Therefore, we should take the value as a reference.

Figure 7 compares the different torques which can be exerted on a star in the propeller regime with $r_{cor} = 0.8r_{mag}$. To calculate $\dot{J}_{CDW}$, we use our Equation (3) and adopt $f_{eff} = 0.2$ and $B_* = 1\,\mathrm{kG}$. Namely, we assume that $\dot{J}_{CDW}$ does not explicitly depend on the stellar spin rate Ω_{ast}. The accretion torque which takes into account the 3D effect, $\dot{J}_{acc} = 0.1\dot{J}'_{acc}$, is also shown. $\dot{J}_{CDW}$ is similar to $\dot{J}_{SW}$ for the given parameter set, which indicates that the conical disk winds can provide as large a spin-down torque as the hypothetical massive stellar winds. If the actual accretion torque is ~$0.1\dot{J}'_{acc}$ or smaller, as suggested by the 3D MHD simulation, the spin-down torques can dominate the spin-up torque. The spin-down torque by magnetospheric ejections is unimportant in this case, but the torque is sensitive to the choice of r_{cor}. If we adopt $r_{cor} = 0.5r_{mag}$, we find that $\dot{J}_{ME} \sim \dot{J}_{CDW}$. Again, we note that the magnitude is likely to be overestimated as the formula for $\dot{J}_{ME}$ is based on axisymmetric models. If magnetospheric ejections are indeed the primary mechanism for angular

momentum transport, we require a theory to account for the observed weak time variability in protostellar accretion.

6. Discussion

Considering the numerical results of ST22, we propose that the magnetically driven winds just around the magnetosphere are key to resolving the spin-down problem. Failed magnetospheric winds, which only appear in three dimensions, significantly reduce the spin-up torque. When a protostar is in the propeller regime, powerful conical disk winds will appear and extract the stellar angular momentum. A combination of the two leads to an efficient angular momentum loss. The mass-loss rate can be ~10% of the accretion rate as a result of direct mass loading from the inner disk to the rotating magnetosphere (Appendix C). Our study shows that a higher accretion rate in the earlier phase leads to a larger wind mass-loss rate. This is the main reason why younger protostars have larger spin-down torque by conical disk wind.

Recent models of spin evolution hypothesize the presence of massive stellar winds (e.g., F. Gallet et al. 2019; L. Gehrig et al. 2022), but this assumption has been challenged from an energetic perspective. Our estimation suggests that, in the propeller regime, conical disk winds will play a critical role in stellar angular momentum loss. If stellar winds play a significant role, the spin-down mechanism will depend heavily on the properties of the accreting object. The detailed spin evolution is influenced by the initial conditions, stellar evolution (e.g., stellar contraction), and disk evolution. Thus, to reach a more robust conclusion, it is essential to incorporate all key factors into a comprehensive model.

In Section 2.2, we have argued that the interaction between the stellar fields and disk fields determines how the mass and angular momentum transfer (see also Appendices A and C). Here, we briefly note the importance of magnetic reconnection between the stellar and disk poloidal fields, which has not been investigated in detail in this study. J. Ferreira et al. (2000) argued that efficient mass loading via magnetic reconnection to the rotating winds will be key in increasing their spin-down torque. On the other hand, M. M. Romanova et al. (2011) performed 2D MHD simulations and showed that magnetic reconnection reduces the accretion torque by decreasing the total magnetic flux of the stellar fields threading the disk (see also K. Parfrey & A. Tchekhovskoy 2017). How the disk fields affect the stellar spin evolution in 3D will be an interesting topic for future studies. As our model (S22) is initialized with a magnetized torus, magnetic reconnection between the stellar and disk poloidal fields will be operating (the presence of the disk fields is a noticeable difference from Z. Zhu et al. 2024). However, a plasma β based only on poloidal fields is much larger than unity in the inner disk outside the magnetosphere, which suggests a minor role of such reconnection in our model.

There are some caveats about our numerical simulations. The 3D simulations of ST22 which motivate this theoretical study have smaller magnetospheric radii (~$2R_*$) than the value used in this study, as we adopted a relatively weak stellar field strength (~160 G) to avoid numerical difficulties. The relation between r_m and r_A for more realistic situations remains to be studied. Another issue is the numerical treatment of the stellar wind. Since the properties of stellar winds remain unclear observationally, it is important to investigate how the results of this study depend on the stellar wind model. A detailed consideration on the efficiency of the conical disk wind f_{eff} is

also necessary. The dependence on the stellar spin will particularly affect the behavior of the star near spin equilibrium. As the efficiency is relevant to turbulent mixing, checking convergence with higher-spatial-resolution simulations also remains an important task.

Studying stellar spin is crucial for testing scenarios of stellar and disk evolution. Observations have revealed the diversity in the structure of protoplanetary disks (J. Bae et al. 2022). Differences in the disk structure will lead to different accretion histories, such as episodic accretion outbursts. As our study indicates the tight relationship between accretion and spin-down, it is possible that the stellar spin distribution is a consequence of the diversity in the disk accretion histories (see also L. Gehrig & E. I. Vorobyov 2023). Stellar spin also affects chemical mixing in the stellar interior, and thus stellar evolution. Lithium may be a good tracer of the history of internal mixing because its abundance is sensitive to it. Some studies suggest that models which take into account the effects of rotational mixing may explain the origin of lithium-depleted stars (J. Bouvier et al. 2016; P. Eggenberger et al. 2022). Accurate interpretation of the stellar surface abundance is important for testing planet formation scenarios because the surface abundance would depend not only on the internal mixing but also on how planet formation affects the abundance of accreting materials (M. Kunitomo et al. 2022). Further studies of spin evolution are thus required for our understanding of how star-planet systems including the solar system are born and evolve.

Appendix A
Analysis of Angular Momentum Flux

We investigate the angular momentum flow around a protostar by analyzing the spatial distributions of the angular momentum flux and toroidal fields on some spherical surfaces. The left column of Figure 8 displays the result at a spherical radius of $r = 2R_*$, which is close to the magnetospheric radius. The Reynolds stress (top panel) takes a large negative value around the midplane, which means that accreting flows are transporting angular momentum inward. We also see some patchy regions with positive values. Some of them correspond to failed magnetospheric winds (see Section 2.2). The Maxwell stress shows positive values in almost all directions (second panel). It takes larger positive values around the midplane because strong toroidal fields exist there in response to the magnetosphere–disk interaction (bottom panel). The sum of the Reynolds and Maxwell stress results in a net spin-down torque (ST22). We note the total flux displays a complicated structure that is highly nonuniform in the azimuthal direction (third panel), which is distinct from the picture based on the axisymmetric model.

The right column of Figure 8 shows the result near the stellar surface, $r = 1.2R_*$. The Reynolds stress displays a spotty structure, which is formed by patchy accretion flows. The Reynolds stress shows negative values only in the northern hemisphere as asymmetric accretion occurs. The Maxwell stress shows large positive values in the range $30° \lesssim |\theta| \lesssim 60°$. The spin-down Maxwell stress is produced by the back-reaction of driving the conical disk winds and failed magnetospheric winds. Indeed, a large part of the stellar field lines driving these winds emanate from the latitudinal range (Figures 2 and 3). The total flux indicates that a large fraction of the spin-up torque by accreting flows is compensated by the magnetic spin-down torque, which results in a smaller rate of angular momentum injection than the classical estimation, $j'_{\rm acc}$.
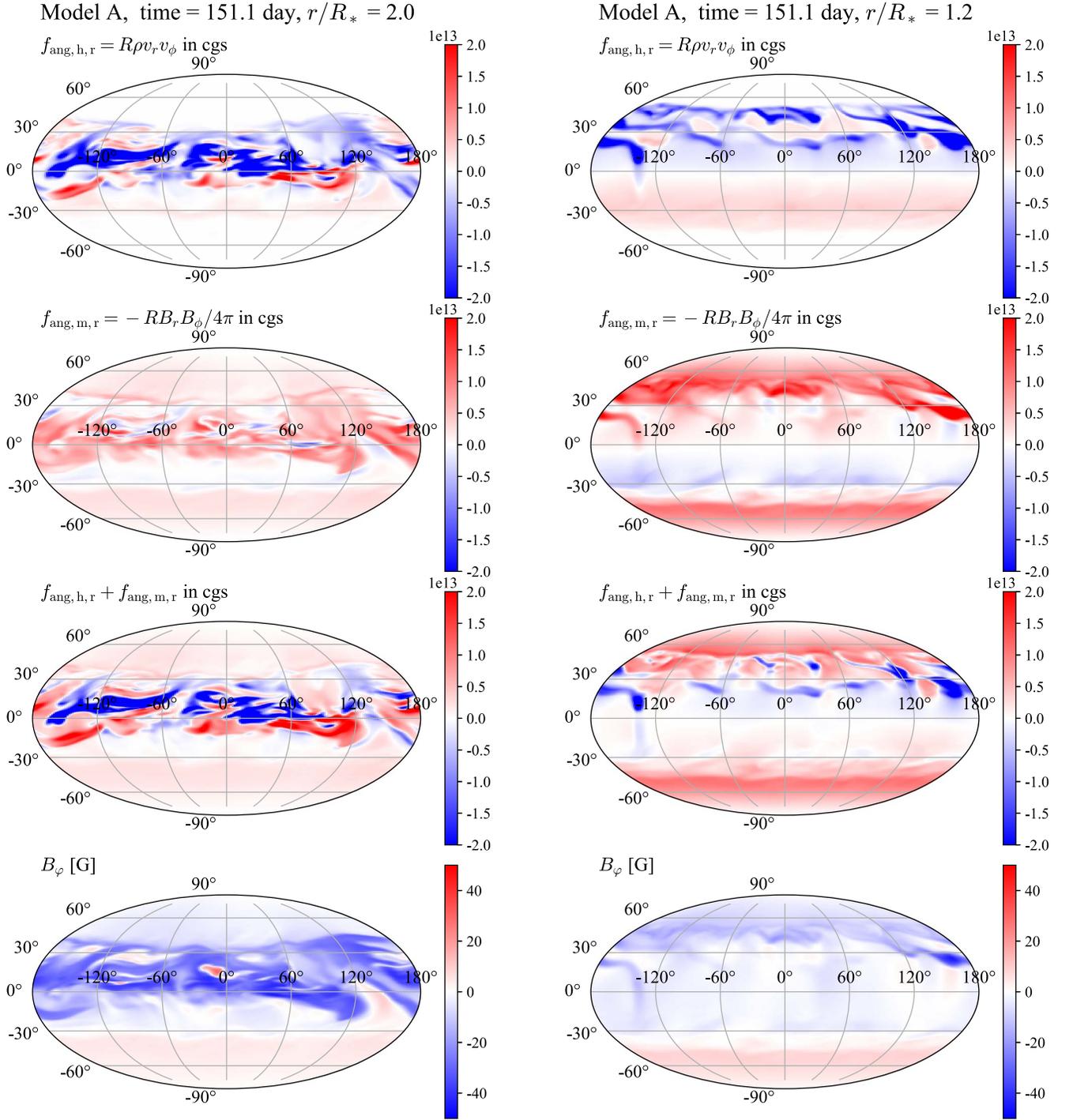
Figure 8. Analysis of angular momentum transfer at $r = 2.0R_*$ (left) and $1.2R_*$ (right) for Model A of ST22. From top to bottom, $f_{\mathrm{ang,h,}r} = R\rho v_r v_\varphi$, $f_{\mathrm{ang,m,}r} = -RB_r B_\varphi/4\pi$, $f_{\mathrm{ang,h,}r} + f_{\mathrm{ang,m,}r}$, and B_φ. Note that accretion mainly occurs in the northern hemisphere.

Appendix B
Structure of the Alfvén Surface

Figure 9 shows the structure of the Alfvén surface. The colors denote the poloidal Alfvén speed $V_{\mathrm{A,p}}$, and the black lines with arrows indicate the averaged poloidal field structure. The magnetosphere expands in the southern hemisphere, and the conical disk wind is blowing along the expanding field lines. The white lines indicate the locations where the poloidal plasma velocity is equal to $V_{\mathrm{A,p}}$. The white line in the conical disk wind region shows the Alfvén surface.

ST22 demonstrates that the outward angular momentum flux takes the largest value around the latitude of approximately $45°$ or slightly larger at the stellar surface (see the right column of Figure 8 of this study and Figure 19 of ST22). Note that the field lines driving the conical disk winds are connected with the northern hemisphere of the star. Considering this result, we focus on the field line emanating from the latitude of approximately $45°$ at the stellar surface. The field line intersects the Alfvén surface approximately at a cylindrical radius of $5R_*$ (see the location indicated by the yellow arrow). As the
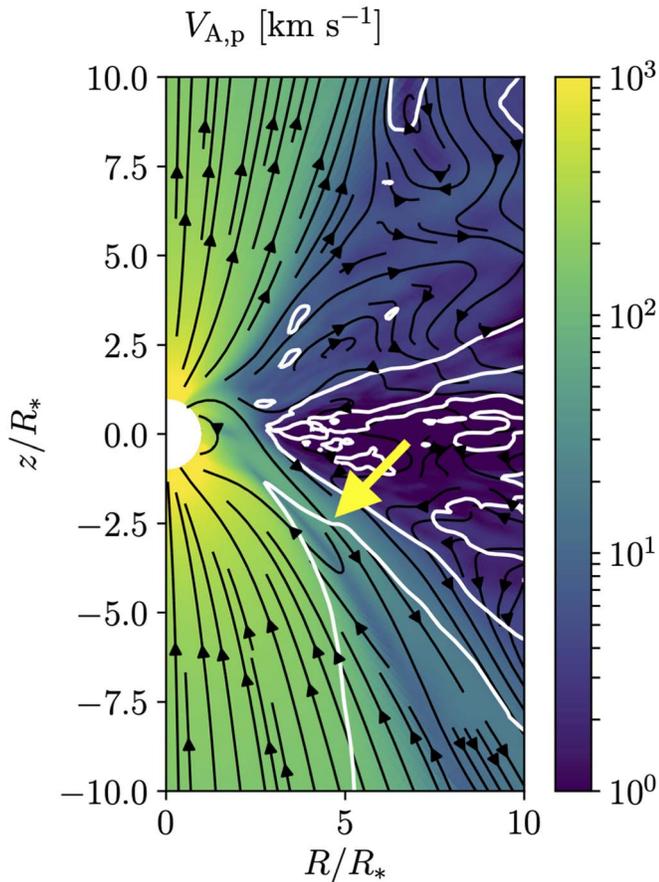
Figure 9. The structure of the Alfvén surface. Colors denote the poloidal Alfvén speed. White contours indicate Alfvén surfaces where the poloidal velocity is equal to the poloidal Alfvén speed. Black lines with arrows denote magnetic field lines projected on this plane. The yellow arrow indicates the location of the Alfvén point discussed in the text of Appendix B. The data are temporally and azimuthally averaged. The time average is performed during the period $t = 190.1$–199.4 days after the simulation starts.

Figure 10. Illustration of the bifurcation of the mass flow. The black arrow indicates the accreting flow in the disk. A fraction of the accreting gas is loaded onto the rotating stellar magnetic fields via turbulence (indicated as yellow arrows) and becomes conical disk wind (orange arrows). The rest of it falls onto the star (dark blue arrow).

magnetospheric radius is approximately $2.5R_*$, we find $r_{\rm A} \approx 2r_{\rm mag}$. Therefore, we adopt $f_{\rm A} = 2$ as a fiducial value in this study. A detailed dependence of the Alfvén radius on the properties of accretion and stellar magnetic fields should be investigated in future studies. The Alfvén surface inside the electric current sheet of the expanding magnetosphere comes closer to the protostar ($\sim 2R_*$). However, because the field strength in the current sheet is weaker than the surrounding field, the angular momentum transport inside the current sheet is unimportant.
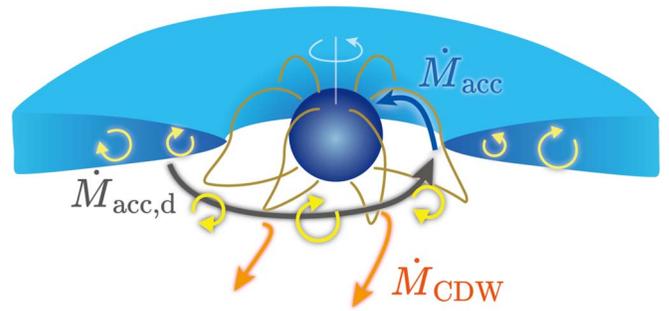
Appendix C
Theoretical Estimation of Mass-loss Rate of Conical Disk Wind

Let us define the accretion rate in the disk as $\dot{M}_{\rm acc,d}$. From the law of conservation of mass, we get

$$\dot{M}_{\rm acc,d} = \dot{M}_{\rm acc} + \dot{M}_{\rm CDW}. \tag{C1}$$

The majority of the accreting material falls onto the protostar as a result of angular momentum loss ($\dot{M}_{\rm acc}$). The rest of it is loaded onto the rotating magnetospheric field via mixing and is ejected away as conical disk wind ($\dot{M}_{\rm CDW}$). Figure 10 displays a

schematic illustration of the bifurcation of the mass flow. Here, we investigate the bifurcation ratio.

We first note the difference in magnetosphere–disk interaction between 2D and 3D models. In 2D models, the accreting material enters the magnetosphere as a result of effective turbulent diffusion (see also the left panel of Figure 1). In other words, accreting material penetrates the magnetosphere as a result of diffusive mixing; in such models, the bifurcation ratio is sensitive to the assumed effective diffusivity and viscosity (G. V. Ustyugova et al. 2006), which are highly uncertain. In three dimensions, the mass loading to the magnetosphere occurs differently. A part of the disk mass is loaded through turbulent mixing at the magnetospheric boundary, which may be modeled using an effective diffusivity as done in 2D models. In addition, the 3D model shows filamentary flows penetrating into the magnetosphere (Figures 3 and 4). These penetrating flows possess strong toroidal fields because they are dragging the disk toroidal fields and continuously shearing them up (see Section 2.2). They retain their coherent structure even in the magnetosphere, possibly because their strong toroidal fields prevent the flows from breaking up. Their coherent structure motivates us to treat the mixing and penetration of the accretion flows separately. The mixing operates mainly at the magnetospheric boundary, which is outside the corotation radius in the propeller regime. Therefore, we expect that most of the gas loaded via mixing will be blown away by a combination of centrifugal and Lorentz forces (G. V. Ustyugova et al. 2006; M. M. Romanova et al. 2009). However, the penetrating flows can enter inside the magnetosphere due to their large inertia.

The bifurcation ratio of the mass flow will depend on the rates of gas penetration and mixing. The rate for the accreting material in the magnetosphere to fall onto the protostar is expressed as $t_{\rm acc,mag}^{-1}$. The rate for mixing (which is essential for mass loading to the conical disk wind) is written as $t_{\rm mix}^{-1}$. By using them, we can write the rate of mass loading to the magnetosphere, $\dot{M}_{\rm load}$, as follows:

$$\dot{M}_{\rm load} = \frac{t_{\rm mix}^{-1}}{t_{\rm mix}^{-1} + t_{\rm acc,mag}^{-1}}\dot{M}_{\rm acc,d}$$
$$= \frac{t_{\rm acc,mag}}{t_{\rm mix} + t_{\rm acc,mag}}\dot{M}_{\rm acc,d}. \tag{C2}$$

A fraction of the loaded mass will be blown away as conical disk wind, while the rest of it will accrete onto the protostar as a funnel flow. By introducing a nondimensional parameter $f_{\rm CDW}$,
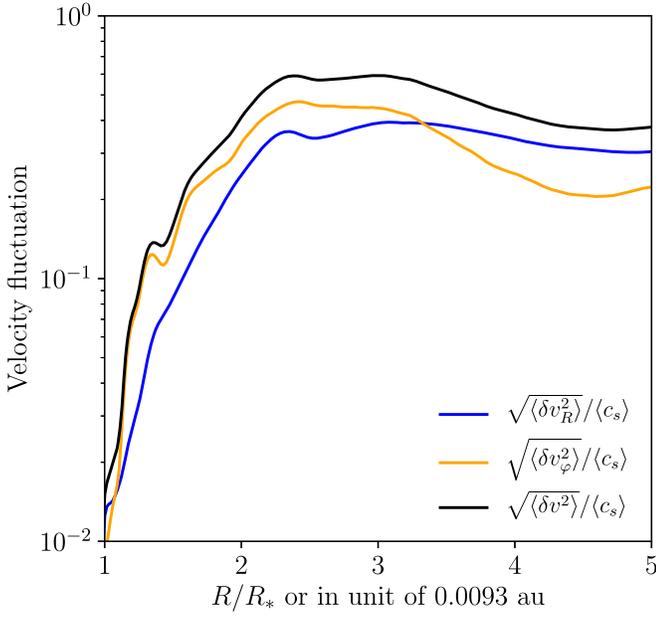
Figure 11. The velocity fluctuation measured around the equatorial plane. The time average is performed during the period $t = 190.1$–199.4 days after the simulation starts.

which denotes the partition rate, we obtain

$$\dot{M}_{\rm CDW} = f_{\rm CDW} \dot{M}_{\rm load}.$$

The value of $f_{\rm CDW}$ should depend on the details of the dynamics (e.g., the distributions of the Lorentz and thermal forces along the field line) and geometrical effects (e.g., north–south asymmetry). Nevertheless, we expect that a large portion of the loaded mass will gain angular momentum from the protostar as the magnetospheric boundary is outside the corotation radius: $r_{\rm cor} < r_{\rm mag}$ (therefore, we expect that $f_{\rm CDW}$ is comparable to unity). This assumption should be examined in future studies. From the law of conservation of mass (Equation C1), we get

$$\dot{M}_{\rm CDW} = \frac{f_{\rm CDW}\, t_{\rm acc,mag}}{t_{\rm mix} + (1 - f_{\rm CDW}) t_{\rm acc,mag}} \dot{M}_{\rm acc}. \qquad (\text{C3})$$

If $f_{\rm CDW}$ is insensitive to the dynamics and geometrical effects at the magnetospheric boundary, this equation explains why $\dot{M}_{\rm CDW}$ is proportional to $\dot{M}_{\rm acc}$.

We estimate $t_{\rm acc,mag}$ and $t_{\rm mix}$ by referring to the results of ST22. As the gas penetrating the magnetosphere falls onto the protostar within 1–2 orbital rotation periods, we take $t_{\rm acc,mag} \approx t_{\rm K}(r_{\rm mag})$, where $t_{\rm K}(r)$ denotes the Keplerian orbital time at the radius of r. The timescale of mixing should be related to the level of the velocity fluctuation (or rms fluctuating velocity) around the magnetospheric boundary, δv. The diffusion coefficient due to turbulence in the Keplerian disk can be expressed as

$$D \approx \frac{1}{3} \frac{\langle \delta v^2 \rangle}{\Omega_{\rm K}}, \qquad (\text{C4})$$

where $\langle \delta v^2 \rangle$ denotes the azimuthally and temporally averaged turbulent velocity. Using this expression, the mixing timescale

can be estimated as

$$t_{\rm mix} = \frac{\Delta R^2}{D}, \qquad (\text{C5})$$

where ΔR is the width of the transition layer between the magnetosphere and the disk.

We measure the velocity fluctuation in the simulation. Figure 11 displays the velocity fluctuation measured around the equatorial plane. The bracket indicates the azimuthally and temporally averaged quantities. δv_R and δv_φ are the radial and azimuthal components, respectively, which are the most relevant to the mixing. c_s is the sound speed. We calculate δv as $\delta v^2 = \delta v_R^2 + \delta v_\varphi^2$. The figure indicates that $\sqrt{\langle \delta v^2 \rangle}/\langle c_s \rangle \approx 0.5$ around the magnetospheric boundary ($R \approx 2.5 R_*$). We note that it is likely the value presented here depends on the numerical resolution. A convergence check is the last remaining task. Nevertheless, we take the measured value as a fiducial value for a better comparison between our simulation and order-of-magnitude calculation. As the vortex size is expected to be limited by the disk thickness or the pressure scale height H, we can rewrite $t_{\rm mix}$ as

$$t_{\rm mix} \approx 4 t_{\rm K}(r_{\rm mag}) \left(\frac{\Delta R}{H} \right)^2 \left(\frac{\sqrt{\langle \delta v^2 \rangle}/\langle c_s \rangle}{0.5} \right)^{-2}, \qquad (\text{C6})$$

where we have used the relation $H = \sqrt{2}\, c_s/\Omega_{\rm K}$.

Using the above parameter sets, we finally find

$$\frac{\dot{M}_{\rm CDW}}{\dot{M}_{\rm acc}} = f_{\rm CDW} \frac{t_{\rm acc,mag}}{t_{\rm mix}} \approx 0.2 \left(\frac{f_{\rm CDW}}{0.8} \right), \qquad (\text{C7})$$

where we set the order-unity parameter $f_{\rm CDW}$ to be 0.8 by considering imperfect mass loading to the conical disk winds. This result indicates that $f_{\rm eff} = 0.1$–0.2 is a reasonable value. A larger $f_{\rm eff}$ may be possible if the velocity fluctuation level is larger than the one considered here (G. V. Ustyugova et al. 2006). Rapid rotators may show a larger fluctuation level because the toroidal fields at the magnetospheric boundary are more strongly amplified than in slow rotators (Figure 11 of ST22). We note that the discussion here only focuses on the bifurcation ratio near the wind-launching region. The above mass-loss rate should be larger than the mass-loss rate of the gas escaping from stellar gravity because not all the wind gas will escape from the system. If the acceleration is insufficient, a fraction of the wind gas will fall back to the disk or the protostar. It is worth noting that the above estimate is close to but a factor of a few larger than the typical ratio of the mass-outflow rate of the jet to the accretion rate (0.05–0.1; see, e.g., M. Fang et al. 2018). We also note that the above discussion ignores the role of magnetic reconnection between the stellar and disk poloidal fields (J. Ferreira et al. 2000). If the reconnection plays a critical role in the mass loading, we will have to consider the effect.

Appendix D
Comparison of Mass Loading between the Stellar Wind and the Conical Disk Wind

Figure 12 compares mass loading between the stellar wind and the conical disk wind. In the case of the stellar wind, the

Stellar wind
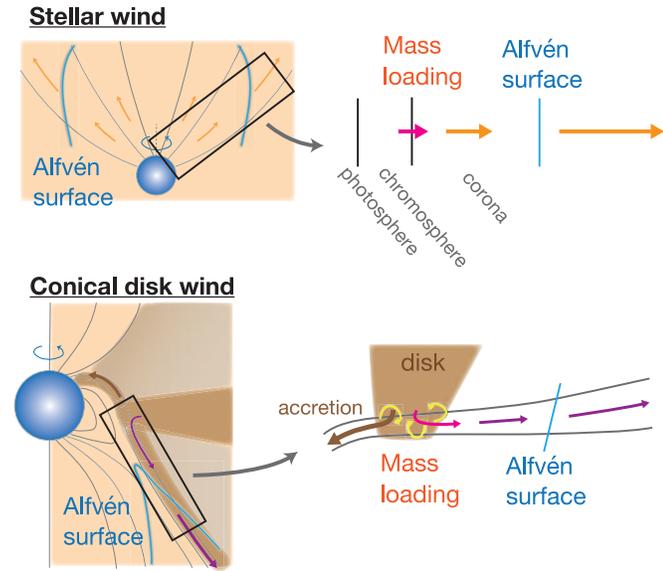
Conical disk wind

Figure 12. Comparison of mass loading between the stellar wind (top) and the conical disk wind (bottom). Note that in both cases mass loading occurs inside the Alfvén surface.

mass is loaded from the stellar atmosphere. This is also true for accretion-powered stellar wind models (S. Matt & R. E. Pudritz 2005; S. R. Cranmer 2008). Coronal gas which passes through the Alfvén surface becomes stellar wind. In the case of a conical disk wind, the wind mass is loaded from the accretion disk at a place distant from the stellar surface. Small-scale magnetic reconnection driven by turbulent motions allows materials to be loaded onto the rotating stellar magnetic fields. In both cases, mass loading occurs inside the Alfvén surfaces. However, in the case of a conical disk wind, the mass is loaded where the gravitational potential is shallower than at the stellar surface. Therefore, blowing the massive wind is less expensive in terms of energy.

J. Ferreira et al. (2000) also note the advantage of the conical disk wind. They studied a situation in which the disk has a poloidal field that can reconnect with the protostellar magnetic fields, which is likely in the early phase of star formation (see also S. Hirose et al. 1997). The reconnection creates a rotating open field and loads the disk gas to the field simultaneously, which leads to the formation of a conical wind mediated by reconnection (which the authors denote a reconnection X-wind). They show that a protostar driving a reconnection X-wind can spin down in a way consistent with observations.

The mass loading in 3D is similar to what is assumed in J. Ferreira et al. (2000) in the sense that magnetic reconnection is relevant. However, the 3D model suggests that the presence of large-scale disk poloidal fields will not be necessary for the reconnection-mediated mass loading. The disk in our 3D model has a finite poloidal field, but the azimuthally averaged poloidal field of the disk appears to be turbulent (see Figure 6 of ST22). Therefore, the strength of the disk field is too weak for the reconnection X-wind to blow. Our study demonstrates that the reconnection-mediated conical disk wind plays important roles in stellar spin-down in a broader situation than previously considered.

Appendix E
Models of Stellar Evolution and Accretion

We calculated the evolution of young stars following M. Kunitomo & T. Guillot (2021). We used the MESA stellar evolution code version 12115 (B. Paxton et al. 2011). We refer the reader to M. Kunitomo & T. Guillot (2021) and the series of papers by Paxton et al. for details of the computational method in this work.

We started from a protostellar phase with a seed of mass $0.1\,M_\odot$. We adopted an accretion rate $\dot{M} = 10^{-5}M_\odot\,\mathrm{yr}^{-1}$ for $t_\mathrm{age} \leqslant t_1$ and $\dot{M} = 10^{-5}M_\odot\,\mathrm{yr}^{-1} \times (t_\mathrm{age}/t_1)^{-1.5}$ for $t_1 < t_\mathrm{age} < 10^7\,\mathrm{yr}$ following L. Hartmann et al. (1998), where $t_1 = 31{,}160\,\mathrm{yr}$ (see Figure 3 of M. Kunitomo & T. Guillot 2021). The resulting final mass is $1M_\odot$. We neglect the effects of rotation and stellar winds on stellar evolution.

We note that the accretion rate $\dot{M}$ is still uncertain. Our fiducial model ($\dot{M} \propto t_\mathrm{age}^{-1.5}$) based on L. Hartmann et al. (1998) seems reasonable from the viewpoint of viscous accretion with a constant viscosity α parameter (N. I. Shakura & R. A. Sunyaev 1973; see discussions in L. Hartmann et al. 1998). However, recent observational studies have suggested another empirical relation in which $\dot{M} \propto t_\mathrm{age}^{-1.07}$ (L. Hartmann et al. 2016). To see the impact of this uncertainty on our conclusion, we have simulated a protostellar evolution with the latter accretion rate. The resulting final stellar mass is $1M_\odot$, as in the fiducial model. Figures 13 and 14 show the evolution of stellar key quantities and spin-down time, respectively, as in Figures 5 and 6. Due to the higher accretion rate in the late phase, this model results in an even shorter spin-down time than the fiducial model in Figure 6 (see also Appendix F). Therefore, we confirm that the conclusion of this study (i.e., the successful spin-down of protostars due to conical disk wind) is not affected by uncertainties in the accretion rate.

The model used in this work is the same as the "K2" model of M. Kunitomo & T. Guillot (2021, their Table 1) except for accretion heating.[8] M. Kunitomo & T. Guillot (2021, their Section 3.1.2) modeled the accretion heating with $\xi = 0.1$, whereas in this study we used $\xi = 0.5$ (i.e., higher-entropy accretion), resulting in the evolution being more similar to the classical case. Since the A_2 parameter, which controls the opacity increase (see their Section 3.1.5), has little impact on the pre-MS radius evolution, we set $A_2 = 0$. We adopted the same input parameters (i.e., initial composition, mixing-length parameter, and overshooting parameter) as the K2 model with $A_2 = 0$ in M. Kunitomo & T. Guillot (2021), which were optimized with solar observational constraints.

The evolution of the magnetospheric radius is described by the scaling of $r_\mathrm{mag} \propto R_*^{12/7} \dot{M}_\mathrm{acc}^{-2/7}$ under the assumption that both B_* and M_* are constant with time. The stellar evolution model shows that

$$\frac{r_\mathrm{mag}}{R_*} \approx 4.3 F(t_\mathrm{age}), \qquad (E1)$$

---

[8] The data and `inlist` files for the MESA simulations are available on Zenodo under an open-source Creative Commons Attribution license: doi:10.5281/zenodo.14524940.
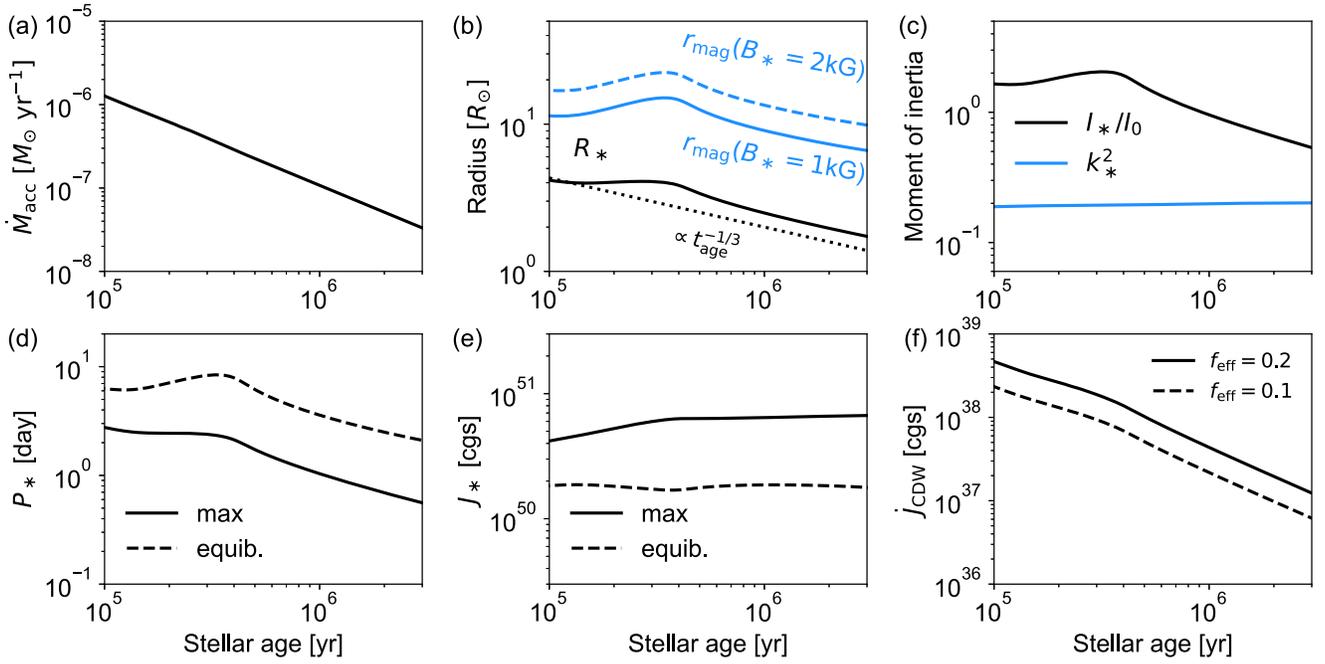
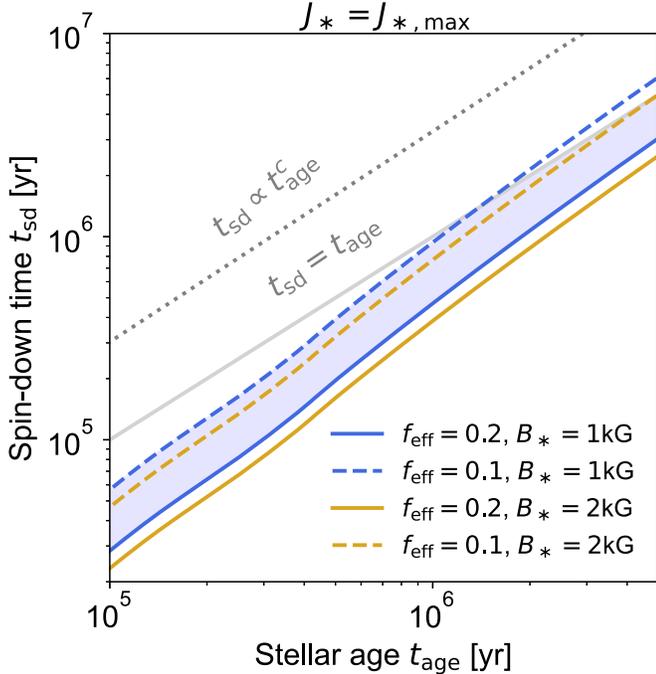**Figure 13.** Same as Figure 5 but with another accretion rate (L. Hartmann et al. 2016).

Figure 14. Same as Figure 6 but with another accretion rate (L. Hartmann et al. 2016).

where $F(t_{age})$ can be described as follows:

$$F(t_{age}) \approx \begin{cases} 1 & \text{Myr} \lesssim t_{age} < 1 \text{ for } 0.3 \text{ Myr} \\ \left(\dfrac{t_{age}}{1 \text{ Myr}}\right)^{0.190} & \text{Myr } t_{age} \geqslant 1 \text{ for .} \end{cases} \quad (E2)$$

The model shows that the value of $F(t_{age})$ is approximately unity in 0.3 Myr $\lesssim t_{age} \lesssim 1$ Myr. We can derive a scaling relation for later evolution by using the relations of $R_* \propto t_{age}^{-1/3}$ and $\dot{M}_{acc} \propto t_{age}^{-1.5}$. Because of the weak dependence of $F(t_{age})$

on time, r_{mag}/R_* slowly changes with time and is of the order of unity in the time range of interest. Therefore, we approximate r_{mag}/R_* as a constant.

This study assumes that stellar contraction occurs owing to the stellar radiation only. But, the conical disk wind also removes energy from the protostar and enhances the stellar contraction (J. Ferreira et al. 2000). Considering the results of J. Ferreira et al. (2000), the stellar radius is insensitive to this effect (at most ∼10%; see their Figure 2). Therefore, our discussion based on the Kelvin–Helmholtz contraction will remain valid even with that effect.

Appendix F
Scaling Relations of Spin-down Time

Using the definitions of $J_{*,max}$ and $\dot{J}_{CDW}$, we can show that $t_{sd,up}$ scales as follows:

$$\begin{aligned} t_{sd,up} &= \frac{0.5 I_* \Omega_K(R_*)}{f_A^2 \dot{M}_{CDW} r_{mag}^2 \Omega_K(r_{mag})} \\ &\propto f_{eff}^{-1} f_A^{-2} B_*^{-2/7} M_*^{15/14} R_*^{-5/14} \dot{M}_{acc}^{-6/7}. \end{aligned} \quad (F1)$$

As the spin-down time $t_{sd,up}$ only weakly depends on the stellar radius, deuterium burning before ∼0.5 Myr has a minor impact on $t_{sd,up}$. At the pre-MS star stage, the stellar mass is nearly constant. If f_{eff}, f_A, and B_* do not significantly change during the evolution, the spin-down time will mainly depend on R_* and $\dot{M}$. In this case,

$$t_{sd,up} \propto t_{age}^{\frac{5}{42} + \frac{6}{7}a} = t_{age}^{59/42}, \quad (F2)$$

for $a = 3/2$. The gray dotted line in Figure 6 indicates this scaling. This scaling is consistent with the results.

It is interesting to note that the spin-down time $(t_{sd,up})$ decreases as the accretion rate increases if the accretion torque is always considerably smaller than the spin-down torque as considered in our model. In the actively accreting phase, the

protostar shows a larger stellar radius and a higher mass-loss rate of conical disk wind. As the spin-down torque is an increasing function of the stellar radius and the wind mass-loss rate, the protostar spins down efficiently in the early phase.

Appendix G
Torques by Magnetospheric Ejection and Stellar Winds

According to F. Gallet et al. (2019), the torque by magnetospheric ejection can be written as

$$\dot{J}_{\rm ME} = K_{\rm ME} \frac{B_*^2 R_*^6}{r_{\rm mag}^3} \left[K_{\rm rot} - \left(\frac{r_{\rm mag}}{r_{\rm cor}} \right)^{3/2} \right], \qquad (G1)$$

where $K_{\rm ME} = 0.21$ and $K_{\rm rot} = 0.7$ are nondimensional parameters calibrated by the 2D MHD simulations of C. Zanni & J. Ferreira (2013). Note that within this formula the torque represents a spin-down torque when its value is negative. As F. Gallet et al. (2019) indicate, the nondimensional calibration parameters are actually not fixed as constants but vary as functions of the model parameters. Given the limited parameter range investigated by C. Zanni & J. Ferreira (2013), we align with their model by adopting a $r_{\rm cor}/r_{\rm mag}$ ratio similar to their results. In the propeller regime of their C01 case, $r_{\rm cor}/r_{\rm mag}$ ranged approximately from 0.77 to 0.94 (see their Table 2). Based on this, we set $r_{\rm cor}/r_{\rm mag} = 0.8$ as the standard value for Figure 7.

The spin-down torque by stellar winds can be expressed as

$$\dot{J}_{\rm SW} = \dot{M}_{\rm SW} r_A^2 \Omega_*, \qquad (G2)$$

where $\dot{M}_{\rm SW}$ is the mass-loss rate of the stellar wind and r_A is the averaged Alfvén radius. Following S. P. Matt et al. (2012), we write r_A as

$$r_A = K_1 \left[\frac{B_*^2 R_*^2}{\dot{M}_{\rm SW} \sqrt{K_2^2 v_{\rm esc}^2 + \Omega_*^2 R_*^2}} \right]^m R_*, \qquad (G3)$$

where $v_{\rm esc} = \sqrt{2GM_*/R_*}$ is the escape velocity, $m = 0.2177$, $K_1 = 1.3$, and $K_2 = 0.0506$. Note that F. Gallet et al. (2019) adopt $K_1 = 1.7$, which is larger than the value given by S. P. Matt et al. (2012). We also assume that the massive stellar wind is powered by accretion via unknown mechanisms and has an efficiency of 10%: $\dot{M}_{\rm SW} = f_{\rm SW} \dot{M}_{\rm acc}$ and $f_{\rm SW} = 0.1$. Note that both the linear relation between $\dot{M}_{\rm SW}$ and $\dot{M}_{\rm acc}$ and the origin of the large efficiency are assumptions and remain elusive.

ORCID iDs

Shinsuke Takasao ● https://orcid.org/0000-0003-3882-3945
Masanobu Kunitomo ● https://orcid.org/0000-0002-1932-3358
Takeru K. Suzuki ● https://orcid.org/0000-0001-9734-9601
Kazunari Iwasaki ● https://orcid.org/0000-0002-2707-7548
Kengo Tomida ● https://orcid.org/0000-0001-8105-8113

References

Armitage, P. J., & Clarke, C. J. 1996, MNRAS, 280, 458
Bae, J., Isella, A., Zhu, Z., et al. 2022, in ASP Conf. Ser. 534, Protostars and Planets VII, ed. S.-I. Inutsuka (San Francisco, CA: ASP), 423
Bai, X.-N., & Stone, J. M. 2013, ApJ, 767, 30
Balbus, S. A., & Hawley, J. F. 1991, ApJ, 376, 214
Blinova, A. A., Romanova, M. M., & Lovelace, R. V. E. 2016, MNRAS, 459, 2354
Bouvier, J., Alencar, S. H. P., Harries, T. J., Johns-Krull, C. M., & Romanova, M. M. 2007, in Protostars and Planets V, ed. B. Reipurth, D. Jewitt, & K. Keil (Tucson, AZ: Univ. of Arizona Press), 479
Bouvier, J., Forestini, M., & Allain, S. 1997, A&A, 326, 1023
Bouvier, J., Lanzafame, A. C., Venuti, L., et al. 2016, A&A, 590, A78
Bouvier, J., Matt, S. P., Mohanty, S., et al. 2014, in Protostars and Planets VI, ed. H. Beuther et al. (Tucson, AZ: Univ. of Arizona Press), 433
Bouvier, J., Sousa, A., Pouilly, K., et al. 2023, A&A, 672, A5
Bryan, M. L., Benneke, B., Knutson, H. A., Batygin, K., & Bowler, B. P. 2018, NatAs, 2, 138
Camenzind, M. 1990, RvMA, 3, 234
Cieza, L., & Baliber, N. 2007, ApJ, 671, 605
Collier Cameron, A., & Campbell, C. G. 1993, A&A, 274, 309
Cranmer, S. R. 2008, ApJ, 689, 316
D'Angelo, C. R., & Spruit, H. C. 2010, MNRAS, 406, 1208
Edwards, S., Strom, S. E., Hartigan, P., et al. 1993, AJ, 106, 372
Eggenberger, P., Buldgen, G., Salmon, S. J. A. J., et al. 2022, NatAs, 6, 788
Fallscheer, C., & Herbst, W. 2006, ApJL, 647, L155
Fang, M., Pascucci, I., Edwards, S., et al. 2018, ApJ, 868, 28
Ferreira, J. 1997, A&A, 319, 340
Ferreira, J. 2013, in Role and Mechanisms of Angular Momentum Transport During the Formation and Early Evolution of Stars, ed. P. Hennebelle & C. Charbonnel (Les Ulis: EDP Sciences), 169
Ferreira, J., Pelletier, G., & Appl, S. 2000, MNRAS, 312, 387
Fiorellino, E., Manara, C. F., Nisini, B., et al. 2021, A&A, 650, A43
Gallet, F., & Bouvier, J. 2013, A&A, 556, A36
Gallet, F., Zanni, C., & Amard, L. 2019, A&A, 632, A6
Gehrig, L., Steiner, D., Vorobyov, E. I., & Güdel, M. 2022, A&A, 667, A46
Gehrig, L., & Vorobyov, E. I. 2023, A&A, 673, A54
Ghosh, P., & Lamb, F. K. 1979, ApJ, 234, 296
Gregory, S. G., Donati, J. F., Morin, J., et al. 2012, ApJ, 755, 97
Hartmann, L., Calvet, N., Gullbring, E., & D'Alessio, P. 1998, ApJ, 495, 385
Hartmann, L., Herczeg, G., & Calvet, N. 2016, ARA&A, 54, 135
Hayashi, M. R., Shibata, K., & Matsumoto, R. 1996, ApJL, 468, L37
Herbst, W., Eislöffel, J., Mundt, R., & Scholz, A. 2007, in Protostars and Planets V, ed. B. Reipurth, D. Jewitt, & K. Keil (Tucson, AZ: Univ. of Arizona Press), 297
Hirabayashi, K., & Hoshino, M. 2016, ApJ, 822, 87
Hirose, S., Uchida, Y., Shibata, K., & Matsumoto, R. 1997, PASJ, 49, 193
Illarionov, A. F., & Sunyaev, R. A. 1975, A&A, 39, 185
Ireland, L. G., Matt, S. P., & Zanni, C. 2022, ApJ, 929, 65
Ireland, L. G., Zanni, C., Matt, S. P., & Pantolmos, G. 2021, ApJ, 906, 4
Jacquemin-Ide, J., Lesur, G., & Ferreira, J. 2021, A&A, 647, A192
Johns-Krull, C. M. 2007, ApJ, 664, 975
Johnstone, C. P., Jardine, M., Gregory, S. G., Donati, J. F., & Hussain, G. 2014, MNRAS, 437, 3202
Kluźniak, W., & Rappaport, S. 2007, ApJ, 671, 1990
Koenigl, A. 1991, ApJL, 370, L39
Kulkarni, A. K., & Romanova, M. M. 2008, MNRAS, 386, 673
Kunitomo, M., & Guillot, T. 2021, A&A, 655, A51
Kunitomo, M., Guillot, T., & Buldgen, G. 2022, A&A, 667, L2
Lii, P. S., Romanova, M. M., Ustyugova, G. V., Koldoba, A. V., & Lovelace, R. V. E. 2014, MNRAS, 441, 86
Lin, M.-K., Krumholz, M. R., & Kratter, K. M. 2011, MNRAS, 416, 580
Livio, M., & Pringle, J. E. 1992, MNRAS, 259, 23P
Long, M., Romanova, M. M., & Lovelace, R. V. E. 2005, ApJ, 634, 1214
Lovelace, R. V. E., Romanova, M. M., & Bisnovatyi-Kogan, G. S. 1999, ApJ, 514, 368
Lynden-Bell, D., & Boily, C. 1994, MNRAS, 267, 146
Matt, S., & Pudritz, R. E. 2004, ApJL, 607, L43
Matt, S., & Pudritz, R. E. 2005, ApJL, 632, L135
Matt, S. P., MacGregor, K. B., Pinsonneault, M. H., & Greene, T. P. 2012, ApJL, 754, L26
McGinnis, P., Bouvier, J., & Gallet, F. 2020, MNRAS, 497, 2142
Mohanty, S., & Shu, F. H. 2008, ApJ, 687, 1323
Ostriker, E. C., & Shu, F. H. 1995, ApJ, 447, 813
Pantolmos, G., Zanni, C., & Bouvier, J. 2020, A&A, 643, A129
Parfrey, K., & Tchekhovskoy, A. 2017, ApJL, 851, L34
Pascucci, I., Cabrit, S., Edwards, S., et al. 2023, in ASP Conf. Ser. 534, Protostars and Planets VII, ed. S. Inutsuka et al. (San Francisco, CA: ASP), 567
Paxton, B., Bildsten, L., Dotter, A., et al. 2011, ApJS, 192, 3

Podio, L., Tabone, B., Codella, C., et al. 2021, A&A, 648, A45

Ray, T., Dougados, C., Bacciotti, F., Eislöffel, J., & Chrysostomou, A. 2007, in Protostars and Planets V, ed. B. Reipurth, D. Jewitt, & K. Keil (Tucson, AZ: Univ. of Arizona Press), 231

Romanova, M. M., Blinova, A. A., Ustyugova, G. V., Koldoba, A. V., & Lovelace, R. V. E. 2018, NewA, 62, 94

Romanova, M. M., Ustyugova, G. V., Koldoba, A. V., & Lovelace, R. V. E. 2004, ApJL, 616, L151

Romanova, M. M., Ustyugova, G. V., Koldoba, A. V., & Lovelace, R. V. E. 2005, ApJL, 635, L165

Romanova, M. M., Ustyugova, G. V., Koldoba, A. V., & Lovelace, R. V. E. 2009, MNRAS, 399, 1802

Romanova, M. M., Ustyugova, G. V., Koldoba, A. V., & Lovelace, R. V. E. 2011, MNRAS, 416, 416

Romanova, M. M., Ustyugova, G. V., Koldoba, A. V., Wick, J. V., & Lovelace, R. V. E. 2003, ApJ, 595, 1009

Safier, P. N. 1999, ApJL, 510, L127

Shakura, N. I., & Sunyaev, R. A. 1973, A&A, 24, 337

Shu, F., Najita, J., Ostriker, E., et al. 1994, ApJ, 429, 781

Suzuki, T. K., & Inutsuka, S.-i. 2009, ApJL, 691, L49

Takasao, S., Tomida, K., Iwasaki, K., & Suzuki, T. K. 2018, ApJ, 857, 4

Takasao, S., Tomida, K., Iwasaki, K., & Suzuki, T. K. 2019, ApJL, 878, L10

Takasao, S., Tomida, K., Iwasaki, K., & Suzuki, T. K. 2022, ApJ, 941, 73

Ustyugova, G. V., Koldoba, A. V., Romanova, M. M., & Lovelace, R. V. E. 2006, ApJ, 646, 304

Uzdensky, D. A., Königl, A., & Litwin, C. 2002, ApJ, 565, 1191

Venuti, L., Bouvier, J., Cody, A. M., et al. 2017, A&A, 599, A23

Zanni, C., & Ferreira, J. 2011, ApJL, 727, L22

Zanni, C., & Ferreira, J. 2013, A&A, 550, A99

Zhu, Z., & Stone, J. M. 2018, ApJ, 857, 34

Zhu, Z., Stone, J. M., & Calvet, N. 2024, MNRAS, 528, 2883